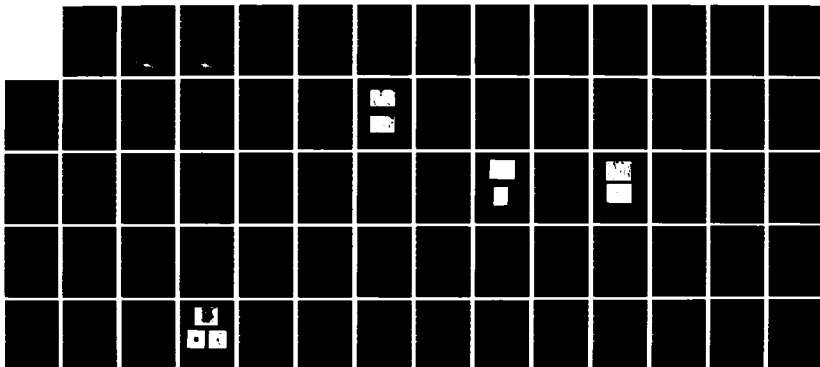MICROSCOPIC STUDY OF THE INFLUENCE OF IMPURITIES ON
INTERFACE BONDING(U) TEXAS UNIV AT AUSTIN CENTER FOR
MATERIALS SCIENCE AND ENGINEERING H L MARCUS 25 JAN 85

UNCLASSIFIED UTCMSE-85-1 N00014-83-K-0143   F/G 11/4   NL
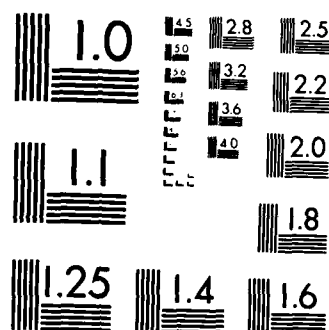
END

FILMED

DTIC

MICROCOPY RESOLUTION TEST CHART

NATIONAL BUREAU OF STANDARDS-1963-A

Center for
Materials Science and Engineering
The University of Texas
at Austin

AD-A151 725

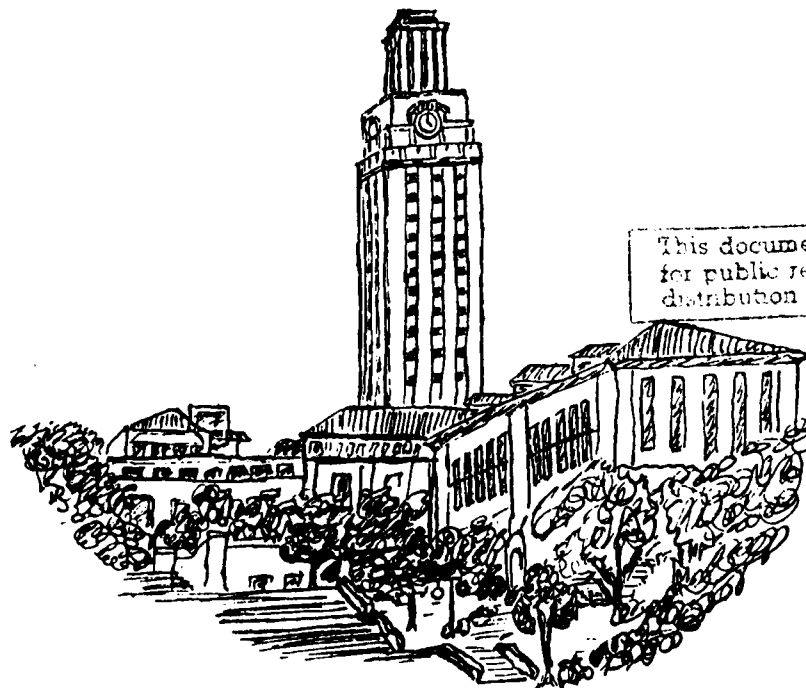MICROSCOPIC STUDY OF THE INFLUENCE OF IMPURITIES ON INTERFACE BONDING

UTCMSE-85-1
Annual Technical Report
January 25, 1985

Office of Naval Research
Contract N00014-83-K-0143

PRINCIPAL INVESTIGATOR: HARRIS L. MARCUS

Mechanical Engineering/Materials Science and Engineering

DTIC FILE COPY

MAR 25 1985

A

85   03   11   085

Center for
Materials Science and Engineering
The University of Texas
at Austin

MICROSCOPIC STUDY OF THE INFLUENCE OF IMPURITIES ON INTERFACE BONDING

PRINCIPAL INVESTIGATOR: HARRIS L. MARCUS

Mechanical Engineering/Materials Science and Engineering

REPORT DOCUMENTATION PAGE		READ INSTRUCTIONS BEFORE COMPLETING FORM
1. REPORT NUMBER UTCMSE-85-1	2. GOVT ACCESSION NO.	3. RECIPIENT'S CATALOG NUMBER
4. TITLE (and Subtitle) Microscopic Study of the Influence of Impurities on Interface Bonding		5. TYPE OF REPORT & PERIOD COVERED Annual Technical Report Dec. 1, 1983 - Nov. 30, 1984
		6. PERFORMING ORG. REPORT NUMBER
7. AUTHOR(s) H.L. Marcus		8. CONTRACT OR GRANT NUMBER(s) N00014-83-K-0143
9. PERFORMING ORGANIZATION NAME AND ADDRESS The University of Texas Mechanical Engineering/Materials Science ETC 5.160, Austin, TX 78712		10. PROGRAM ELEMENT, PROJECT, TASK AREA & WORK UNIT NUMBERS
11. CONTROLLING OFFICE NAME AND ADDRESS Office of Naval Research Metallurgy and Ceramics Program Arlington, VA 22217		12. REPORT DATE January 25, 1985
		13. NUMBER OF PAGES 63
14. MONITORING AGENCY NAME & ADDRESS(if different from Controlling Office) Dr. B.A. MacDonald, Metallurgy Division Office of Naval Research, Code 471 Department of the Navy Arlington, VA 22217		15. SECURITY CLASS. (of this report) UNCLASSIFIED
		15a. DECLASSIFICATION/DOWNGRADING SCHEDULE

16 DISTRIBUTION STATEMENT (of this Report)

Approved for public release; Distribution unlimited.

17. DISTRIBUTION STATEMENT (of the abstract entered in Block 20, If different from Report)

18. SUPPLEMENTARY NOTES

19. KEY WORDS (Continue on reverse side if necessary and identify by block number)

Auger Electron Spectroscopy, Interface Characteristics, Interface Fracture, Scanning Auger Microscopy, I/V Switching, Metal Matrix Composites, Aluminum/Graphite Composites, Mn Stainless Steels, Intergranular Fracture.

20 ABSTRACT (Continue on reverse side if necessary and identify by block number)

Research on the relation between impurities and second phases at interfaces and their impact on the mechanical properties is reported. Model layered systems involving interfaces in Al/graphite MMC and the Ni-Ni system were investigated. In addition model steel systems, both ferritic and austenitic were studied to evaluate segregation to the interface and the impact on fracture and stress corrosion cracking of the segregated species.   (Continued)

DD FORM 1473 EDITION OF 1 NOV 65 IS OBSOLETE

In the layered structures the relation between the conductivity normal to the interface and the fracture path was evaluated under different interface processing conditions with a variety of experimental results. The method of preparation of the interface played a major role in the switching and fracture characteristics.

In the steels a correlation between the segregation at the interface and the fraction of interface failure with the fracture toughness was evaluated.

TABLE OF CONTENTS

Microscopic Study of the Influence of Impurities
on Interface Bonding

I. Introduction

In the previous annual reports (1,2), two major experimental areas were emphasized. The primary research area was involved in the detailed evaluation of the fracture behavior of specially prepared interfaces and the impact changes in chemistry and electrical characteristics have on that behavior. The second major thrust was the investigation of the interfaces in discontinuous silicon carbide - aluminum metal matrix composites. During the past year the research on the fracture of model laminate systems has continued. In addition, studies of model systems of iron based alloys have been started to evaluate the impact of impurities localized at interfaces on their mechanical behavior. These include body centered cubic alloy and Mn stabilized face centered cubic stainless steels.

II. Background

In all cases of structural materials the interface chemistry and bonding of interfaces, phase boundaries and grain boundaries play a major role in the fracture behavior. An example is the interface role in the bonding characteristics of the Al/Gr layered system. The interface strength of this system has been observed to be dependent on the thickness of the aluminum oxide layer (3). When the oxide films are thin, the interface is more adhesive and strongly bonded to the graphite. As the oxide thickness is increased the

bond between the oxide and the graphite is weakened, as indicated by a change in fracture path. Another important characteristic of this particular interface structure is its threshold switching behavior. Threshold switching can be described as an abrupt change in resistivity of the structure when it is subjected to sufficiently high electric fields (4). When the voltage is increased above a certain threshold voltage, the resistivity abruptly decreases and will remain in the low resistivity state for some relaxation time.

One of the purposes of this research is to study the interrelationship between the threshold switching characteristics and the mechanical strength of the interfaces and the impact of impurities on this behavior. Model systems can be constructed through vapor deposition of thin layers to build the appropriate interface region. By introducing a thin layered model the investigation of the correlation between electronic and mechanical properties of the system is greatly simplified. This structure allows the easy application of voltage across the interface which under the proper conditions produces threshold switching to a higher conductivity state and also makes it convenient for testing the mechanical strength of the interface. A force normal to the interface is applied, exposing the location of the weakest interface. The determination of the composition of the exposed surface is made with the aid of surface sensitive Auger electron spectroscopy (AES). This type of analysis has revealed that when a high conductivity interface state exists the adhesion of the interface between $\gamma-Al_2O_3$ and the graphite crystal is changed from that observed for the condition of the low conductivity interface state (3,5).

In addition to studies on the Al/graphite laminate structures,
studies of interfaces on Ni substrates have also been started.
These are coupled to studies of impurity related intergranular failure
of stable austenite stainless steels under stress corrosion cracking
conditions. Some model stainless steels were made and an investiga-
tion into intergranular cracking is underway. A limited study relating
the fracture mode and the apparent fracture toughness to impurity
segregation in iron ternaries was also performed. This was an exten-
sion of some previous work based on embrittlement in steels (6)
and a nonequilibrium model for the fracture (7,8).

The results to date of the above studies will be outlined in
the following sections with greater detail presented in the appendices.
Appendix A covers the results to date in the impurity effects on
the interfacial strength of steels; Appendix B covers the Ni laminate
systems and Appendix C describes the continued effort on the Al/
graphite layered structures. Appendix D is a paper on a technique
for choosing a dispersoid with a maximum elastic constant for use
within a composite system.

III. Experimental Results and Discussion

A. Impurity Effects on the Interfacial Failure in Steels

Replacing Ni in the austenitic stainless steel by Mn and N,
offers an improvement in the Intergranular Stress Corrosion Cracking
(IGSCC) behavior of the alloys. High resistance to IGSCC in the
Cr-Mn-N stainless steel can be developed by controlling the alloying
elements and impurities. The objective of this research is to deter-
mine how the alloying element, Mn and impurities, P and S influence

the IGSCC in the chloride environment. This study is coupled to
the Ni layered interface failure studies.

Two series of alloys: 18Cr-18Mn series, 18Cr-13Mn series,
with different impurities (P,S) levels were specially made by Armco,
Inc. In addition to these four alloys, commercial alloys including
Armco's Nitronic 33 will also be tested and evaluated for comparison.
Details of the alloys and sample preparation are given in Appendix
A.

The main results to date were associated with characterization
of the precipitation reaction and grain size development in both
the special alloys and the commercial alloys. The most detailed
microstructural study was on an 18Cr-18Mn commercial steel. Electro-
chemical tests showed a heat treatment dependence of the passivity
and pitting potentials of the alloys. Aged specimens showed a higher
susceptibility to pitting in ferric chloride solution than the as-
quenched specimen. In all cases tested to date the base metal did
not show significant susceptibility to IGSCC, but welded sections
did have intergranular cracks. The level of P and S at the grain
boundaries for the samples tested has not yet been established unam-
biguously.

The studies on the ferrite model systems of Fe-P, Fe-Mn-P,
Fe-Mo-P and Fe-W-P concentrated on determining the fracture mode
and how it related to the cosegregation of P and the alloying elements
to the grain boundaries. The following results were obtained and
are an extension of previously reported results (8).

1. The change in the critical stress intensity factor as a function
    of embrittlement which is represented by percent intergranular

failure and the grain boundary P concentration is similar to the change in the bending stress, and the local critical stress as a function of percent intergranular failure.

2. The critical stress intensity factor decreases with increasing percent intergranular failure.

3. The additive embrittling effect of Mn on the P segregation is seen in the K_{eff} vs. aging time and K_{eff} vs. percent intergranular failure.

4. The remedial effect on the P embrittlement of Mo and W is seen in the K_{eff} vs. aging time plots.

5. The type of transgranular fracture found to occur in a majority of specimens was cleavage with some specimens possibly fracturing in a quasi-cleavage mode.

6. From the specimens sampled, where intergranular fracture was observed, fairly clean grain boundary facets with scattered signs of minor deformation could be seen.

7. The low amount of plastic deformation suggests that the test temperatures chosen were suitable at eliminating gross amounts of plastic deformation.

The metallographic and fracture mechanics analysis results complement the more detailed results presented previously and are presented in more detail in Appendix A.

B. Impurity Effects on Ni-Ni Interfaces

Ni-Ni and Ni-NiO-Ni systems have been chosen since nickel is a face centered cubic structural material as well as it being an important addition to many other structural alloy systems. In addition

there are less complications with formation of the natural oxide
of Ni. NiO is an important oxide system in electronic packaging
and the selection of NiO gives one the opportunity to study the
transition metal oxides and their related electronic switching proper-
ties. The Ni substrate initially used was a polycrystalline rod
.9999% pure with an average grain size of 50 μm. Oxidized specimens
were made by heating the specimen in a tube furnace. The deposited
Ni thin film overlays were made in a 1×10^{-6} torr vacuum. The elec-
tronic switching of the Ni-NiO specimens is hard to characterize.
Switching was not observed in the Ni-Ni specimens for oxide
nesses up to 1.0 μm thick at the interface. Since this research
is primarily concerned with very thin interfaces (monolayers anu
up to 100 Å), switching may not be relatively important in this
system. More details of this work are presented in Appendix B.

C. Interface Failure in Al/Graphite MMC

The research in this report was aimed at cleaning up the reactive
atmosphere, verifying the structural characteristics of the evaporated
oxide film, and making a quantitative measure of strength changes
in the planar composites. Details are presented in Appendix C.

Substrates of Ticonderoga single crystal graphite having a
[0001] surface normal were used to create the interface. Oxide
thicknesses deposited on the graphite averaged 25 nm while the aluminum
overlayers averaged 100 nm. In addition to reactively evaporated
oxides, some aluminum oxides were produced by depositing aluminum
on the substrates and resistively heating the tantalum mask in an

atmosphere of oxygen at a pressure of 10^{-4} Torr. By depositing

the oxide film on transmission electron transparent single crystal

graphite the film structure was studied directly in the TEM. In

every case the oxide film was amorphous as determined by electron

diffraction. The presence of aluminum and oxygen was verified by

electron energy loss spectroscopy (EELS). Preliminary results of

a semiquantitative analysis of the EELS spectra showed that the

oxide's composition was in the ratio of Al_2O. The oxides transformed

to 10 nm crystallites of gamma-Al_2O_3 after long exposure to the

electron beam. The electrical characteristics of the reactively

evaporated films were ohmic with high conductivity. In contrast

to the reactively evaporated films, the thermally oxidized films

showed stable reproducible switching of a different type. The switching

observed in the anodic oxides is known as voltage controlled N-type

switching and the switching observed in reactively evaporated oxides

is known as current controlled S-type switching. Details of the

two types are given in Appendix C.

The high state of conductivity observed in our evaporated oxide

films may result either from a very high impurity concentration

or from a deviation of oxide stoichiometry. Auger spectroscopy

indicates that the former is unlikely. If excess oxygen was present

in our oxides, the off-stoichiometric proportions of cations and

anions would create a greater concentration of charge carriers per-

mitting the high electrical conductivity state.

As discussed previously, switching was not observed with the

oxides in this study. Failure, however, did occur at the oxide-
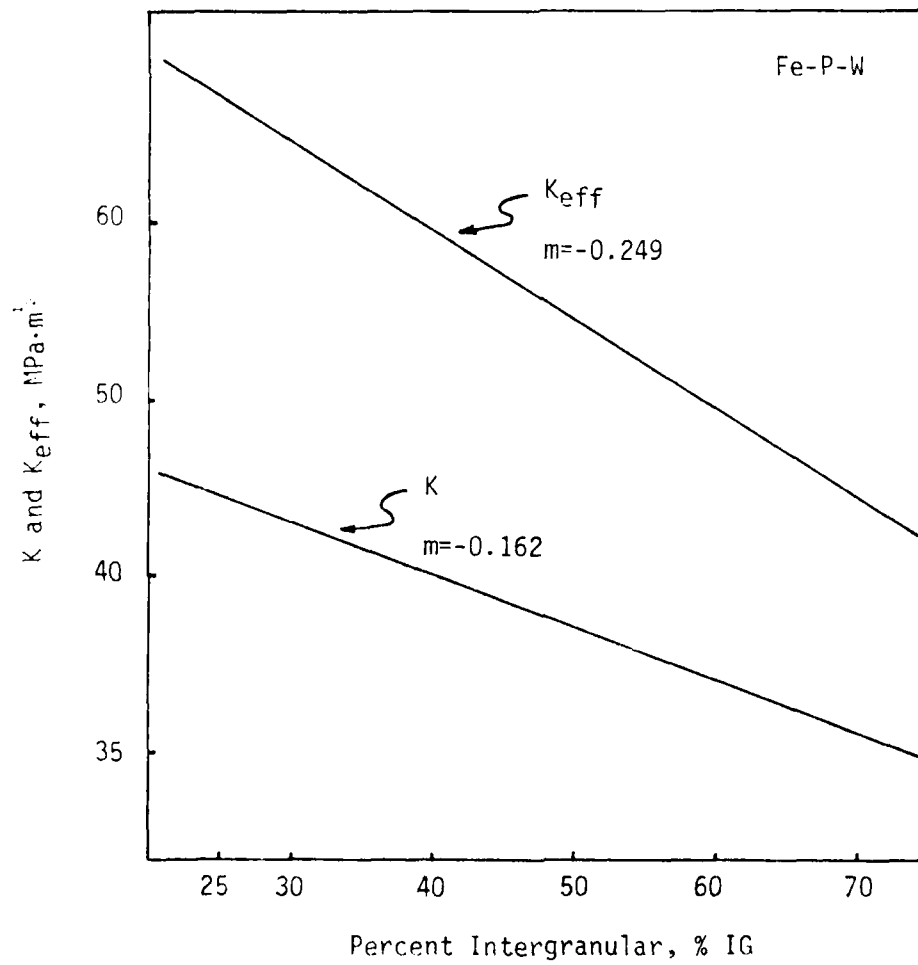
Figure A.10 Variation of K and plane stress K_{eff} with % IG for the Fe-P-W specimens.
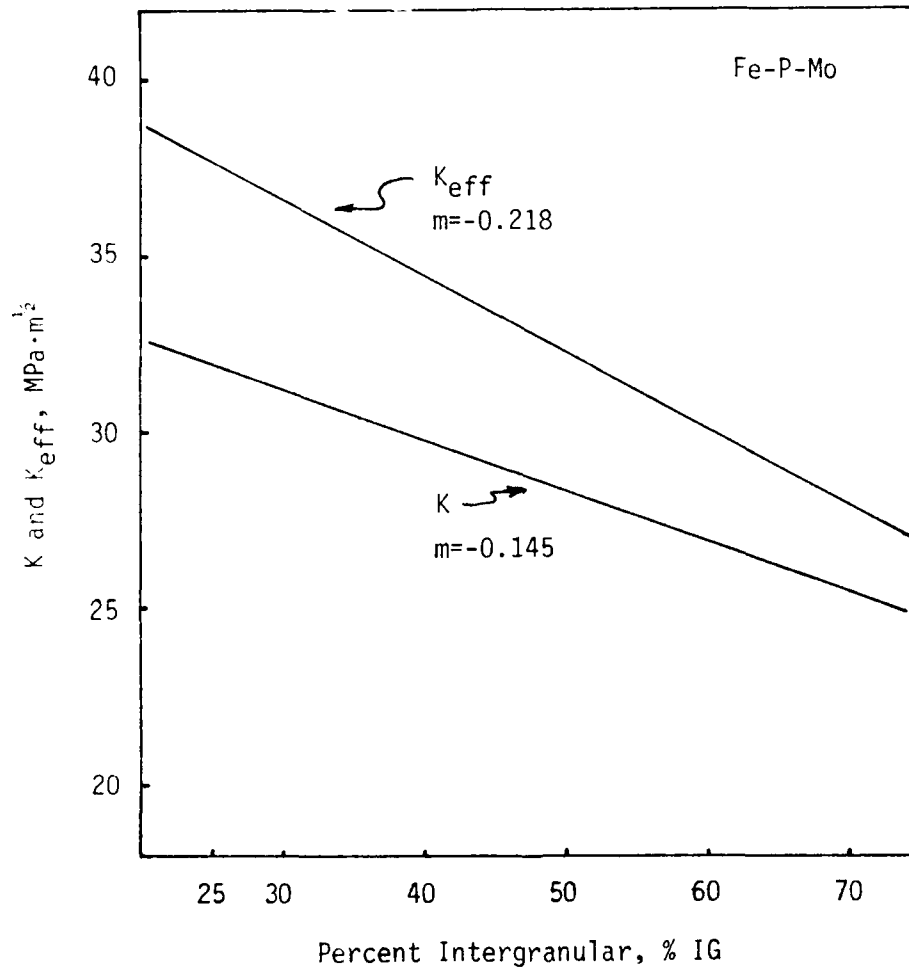
Figure A.9   Variation of K and plane stress K_{eff} with % IG
             for the Fe-P-Mo specimens.
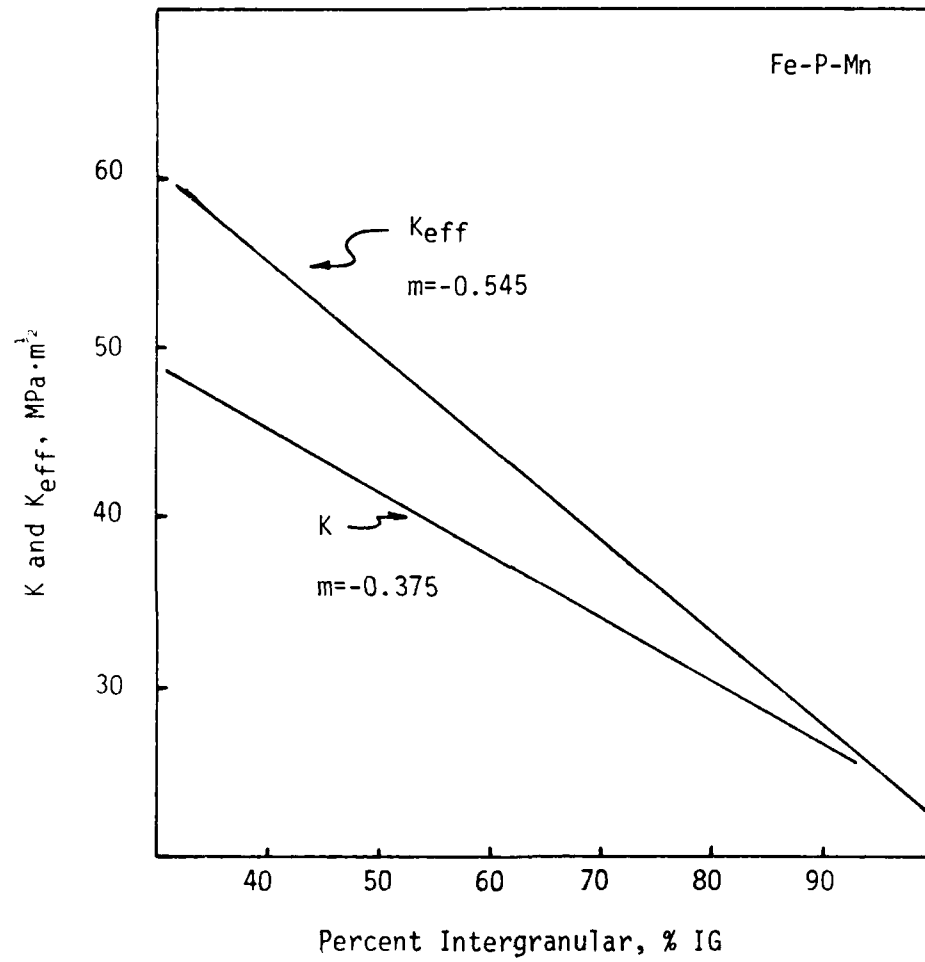
Figure A.8   Variation of K and plane stress K_{eff} with % IG
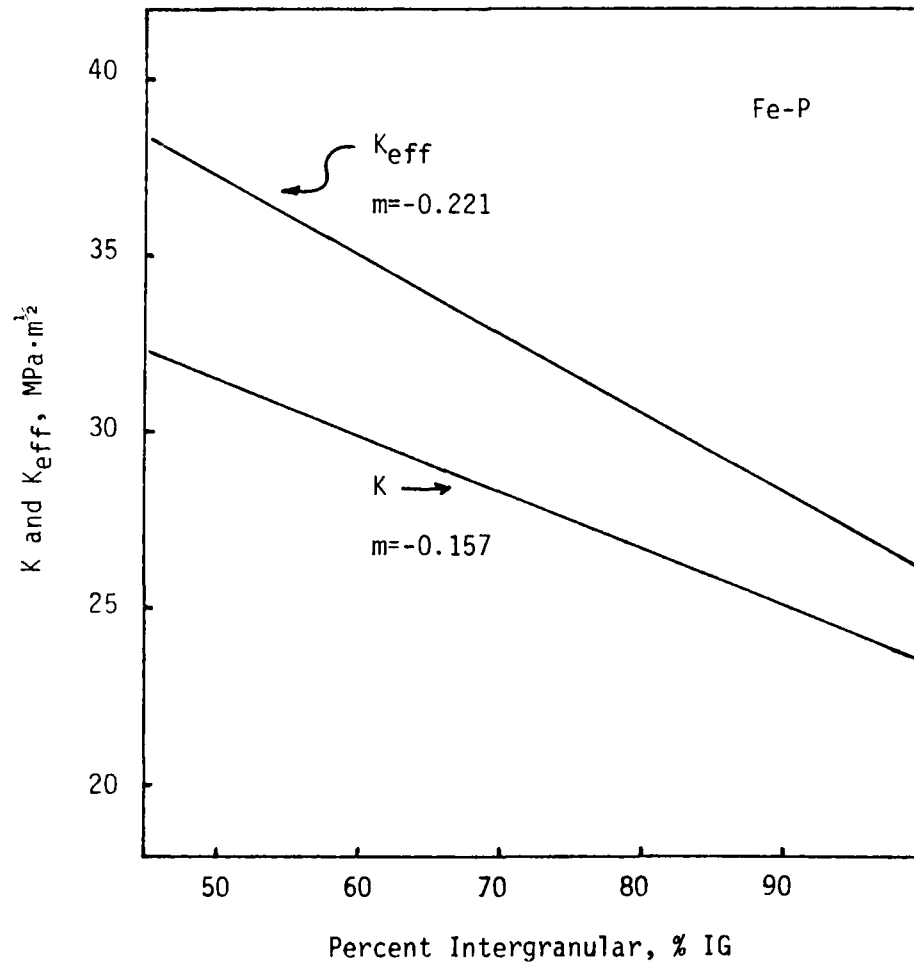   for the Fe-P-Mn specimens.

Figure A.7   Variation of K and plane stress K_{eff} with % IG
for the Fe-P specimens.

Fe-P-Mn, Fe-P-Mo, and Fe-P-W specimens respectively, heat treated at 500 C. K_{eff} is the plane   stress intensity factor and %IG is the measured amount of intergranular fracture. From these curves it can be seen that Mn acts as an embrittler while Mo and W reduce embrittlement. Figures A.7-A.10 show the variation of K and the plane stress K_{eff} with % IG for the respective alloy systems. K is the 4-point bend test stress intensity factor (A1). These curves show that the stress intensity factor decreases with increasing % IG for the various alloy systems.

3. Results

Based upon the observation of the 4-point bend tests fractographs and the evaluation of the Linear Elastic Fracture Mechanics analysis, the following results were determined:

1. The type of transgranular fracture found to occur in a majority of specimens was cleavage with some specimens possibly fracturing in a quasi-cleavage mode.

2. From the specimens sampled, where intergranular fracture was observed, fairly clean grain boundary facets with scattered signs of minor deformation could be seen.

3. The low amount of plastic deformation suggests that the test temperatures chosen were suitable at elimaniting gross amounts of plastic deformation.

4. The change in the stress intensity factor as a function of

Figure A.5   Variation of plane stress K_{eff} and % IG with aging
time for Fe-P-Mo specimens heat treated at 500°C.

Figure A.6   Variation of plane stress K_{eff} and % IG with aging
time for Fe-P-W specimens heat treated at 500°C.

AS

Figure A.3   Variation of plane stress K_{eff} and % IG with aging
time for Fe-P specimens heat treated at 500°C.
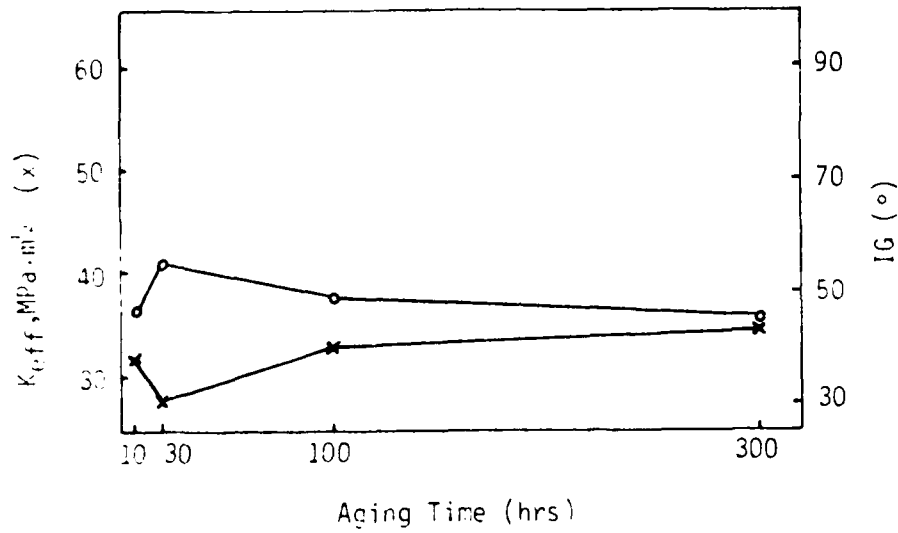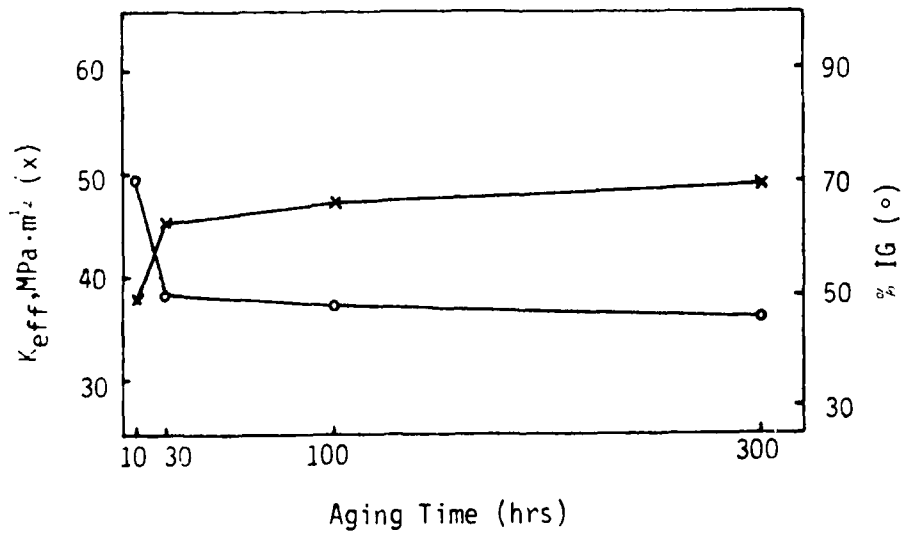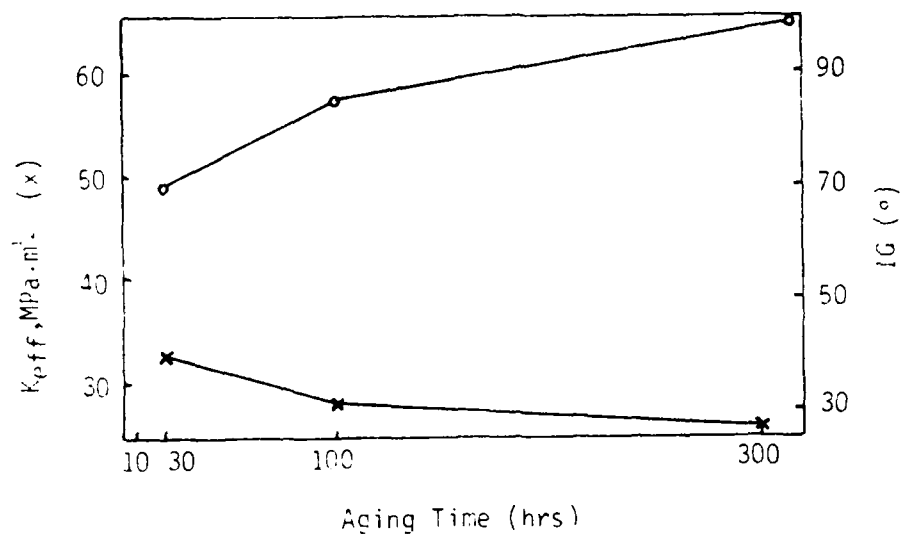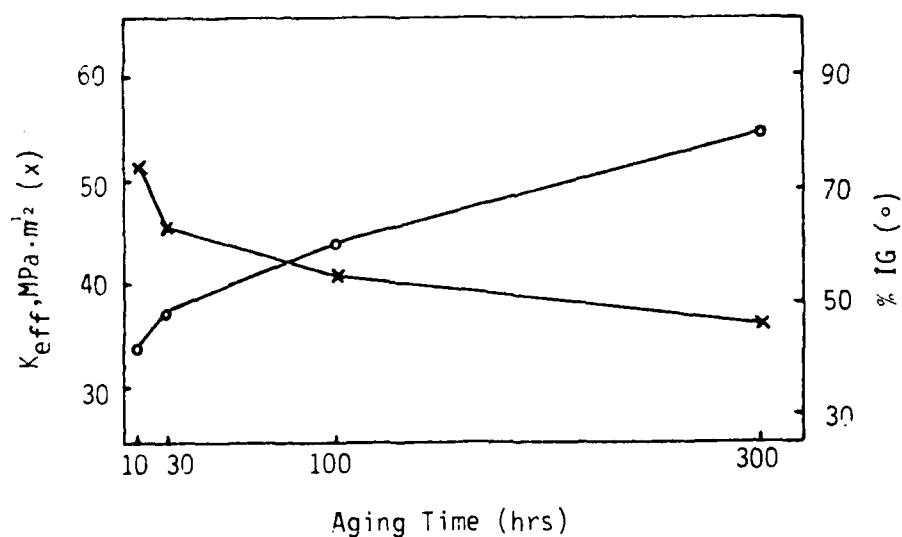

Figure A.4   Variation of plane stress K_{eff} and % IG with aging
time for Fe-P-Mn specimens heat treated at 500°C.

Figure A.1 Fractograph of specimen 05503, an Fe-P specimen heat
treated at 550°C for 30 hrs.,which had 75% inter-
granular failure.

Figure A.2 Fractograph of specimen 25503, an Fe-P-Mo specimen heat
treated at 550°C for 30 hrs., which had 26% intergran-
ular failure.

modification of the fracture surface as determined by fractography and a Fracture Mechanics analysis.

Table A.2

type of alloy | aging temperature | aging time

| X | XX | XX |

type of alloy   aging temperature   aging time

0: Fe-P   40: 400 C   0: 0

1: Fe-P-Mn   45: 450 C   01: 10 hrs.

2: Fe-P-Mo   50: 500 C   03: 30

3: Fe-P-W   55: 550 C   10: 100

                     60: 600 C   30: 300

2. Experimential Approach

The specimens were annealed, tempered, and aged to aquire various degrees of segregation. Tensile tests and 4-point bend tests were run at low temperatures to obtain fracture surfaces showing little if any small scale yielding. SEM was performed on the 4-point bend test fracture surfaces. A Linear Elastic Fracture Mechanics analysis of the 4-point bend tests was conducted to evaluate the effects of the grain boundary segregated P and alloying elements. Figures A.1 and A.2 show typical fractographs of specimens tested in 4-point bending. Figures A.3-A.6 show the variation of plane stress K_{eff} and % IG with aging time for Fe-P,

2. Mn, Mo, and W were chosen as alloying elements because it has been suggested that Mo and W have remedial effects on P grain boundary segregated induced grain boundary embrittlement and that Mn has embrittling effects on P grain boundary induced grain boundary embrittlement.

3. These alloys have little or essentially no carbon, thereby avoiding the effects of carbon segregation to the grain boundary as elemential carbon or more complex carbides.

4. The binary system was chosen for comparison reasons so that segregation and embrittlement could be investigated without the effects of the alloying elements.

Table A.1

Alloy I.D.	Elements (wt. %)		
0	0.057-0.1P		(bal.) Fe
1	0.1P	2.6 Mn	" "
2	"	3.2 Mo	" "
3	"	4.6 W	" "

These alloys were given the specimen designations according to composition and aging heat treatment as shown in Table A.2. Metallography and microscopy were conducted to verify uniformity of grain size. AES of the fractured specimens and thermodynamic modeling of the segregation were conducted in a previous study (A2). This study focuses on the

Appendix A

Introduction

In this appendix the study of interface modification on the failure of engineering materials will be described in two sections. Section AI investigates interface (grain boundary) fracture of four Fe-P alloys; the binary system and three ternary alloys which have Mn, Mo, and W additions respectively. The principle objectives of this research are to determine how grain boundary fracture morphology is effected by the segregation of the impurity P, as well as the segregation of the alloying elements. Section A II focuses on intergranular failure of Fe-Cr-Mn-N alloys with controlled P and S content. The objectives are to determine how the impurties (P and S) and the alloying elements (Mn, Cr, and N) are related to the intergranular stress corrosion cracking (IGSCC) in the chloride environment.

Both research sections involve extensive specimen preparation, mechanical testing, metallography and microscopy, SEM and/or AES analysis, as well as other experimential techniques. This appendix is divided into the two respective sections with the results cited independently by section.

Section AI. Mn,Mo, and W Influence on P Grain Boundary Embrittlement

1. Material Description

The alloy systems chosen for this research are listed in Table A.1. These alloy systems were chosen for the following reasons (A1-A3):

    1. P is a common impurity in commercial Fe alloys that is related to grain boundary failure.

V. References

1. Harris L. Marcus, Final Technical Report UTMSE-83-1, "Interface Character of Aluminum-Graphite Metal Matrix Composites," January 1983, ONR Contract N00014-78-C-0094.

2. Harris L. Marcus, Annual Technical Report UTCMSE-84-1, "Microscopic Study of the Influence of Impurities on Interface Bonding," January 1985, ONR Contract N00014-83-K-0143.

3. Swe-Den Tsai, Ph.D. dissertation, The University of Texas at Austin, 1980.

4. D.F. Weirauch, Appl. Phys. Letters 16 (1970) p. 72.

5. H. Mendez, D. Finello, R. Walser and H.L. Marcus, "Correlation of Electronic State and Fracture Path of Al/Graphite Interfaces," Scripta Met. 16 (1982) p. 855.

6. D.Y. Lee and H.L. Marcus, "Grain Boundary Embrittlement in Steels," in Treatises in Metallurgy, TMS-AIME, J. Tien and J. Elliot, eds., 571 (1981).

7. J.P. Stark and H.L. Marcus, "The Influence of Segregation on Grain Boundary Cohesion," Met. Trans. 8A, 1423 (1977).

8. D.Y. Lee, E.V. Barrera, J.P. Stark and H.L. Marcus, "The Influence of Alloying Elements on Impurity Induced Grain Boundary Embrittlement," Met. Trans. 15A, 1415 (1984).

the Ni-Ni system were investigated. In addition model steel systems, both ferritic and austenitic were studied to evaluate segregation to the interface and the impact on fracture and stress corrosion cracking of the segregated species.

In the layered structures the relation between the conductivity normal to the interface and the fracture path was evaluated under different interface processing conditions with a variety of experimental results. The method of preparation of the interface played a major role in the switching and fracture characteristics.

In the steels a correlation between the segregation at the interface and the fraction of interface failure with the fracture toughness was evaluated.

graphite interface. This is consistent with failure in the high conductivity state of earlier studies.

Our present work has produced suggestive evidence of the causal relationship between electrical and fracture characteristics. A blueish appearance of the graphite fracture surface was observed after interfacial failure in the high conductive state. Subsequent AES indicated no oxide present on this surface eliminating refraction from thin layers as a possible cause. The blueish color change has been observed in intercalation studies of single crystal graphite and is associated with the reduction of the graphite (i.e., electron deficient). This viewed in the context of the previously discussed catalytic effect of the aluminum oxide on graphite presents some interesting possibilities that are being pursued.

As part of the interface studies the mechanical strength of the interface is being probed. Both direct tensile tests and laser induced shock wave loading are being evaluated. Details of all of the above are given in Appendix C.

A side issue that was investigated was how to predict the modulus of potential dispersoids in alloy systems. Appendix D describes a correlation of the elastic moduli with the melting temperature of the potential dispersoids.

IV. Summary

Research on the relation between impurities and second phases at interfaces and their impact on the mechanical properties is reported. Model layered systems involving interfaces in Al/graphite MMC and

embrittlement which is represented by percent intergranular
failure is similar to the change in the bending stress, and the
local critical stress (A3), as a function of % IG.

5. The stress intensity factor decreases with increasing % IG.

6. The embrittling effect of Mn is seen in the K_{eff} vs. aging time
and K_{eff} vs. percent intergranular failure.

7. The remedial effect of Mo and W is seen in the K_{eff} vs. aging
time plots.

Section A II   Intergranular Stress Corrosion Cracking (IGSCC) of
Austenitic Cr-Mn-N Stainless Steels in the chloride
environment with varying S and P content

Many investigation on the stress corrosion cracking (SCC)
characteristics of Cr-Ni austenitic stainless steel have been
reported to be susceptible to a chloride environment(A4). Replacing
Ni in the austenitic stainless steel by Mn and N, the resistance to
SCC could be improved. It was also suggested that high resistance
to SCC in the Cr-Mn-N stainless steel can be developed by
controlling the alloying elements and impurities (A5). The objective
of this research is to determine how the alloying element, Mn and
impurities, P and S influence the IGSCC in the chloride environment.
This reports on research completed in 1984 and describes
experiments to be performed in 1985.

1. Research materials selection

The materials are selected according to the following requrement.

a. stable, single phase austenite
b. strong resistance to SCC in chloride environment
c. low pitting corrosion
d. less sensitization
e. high strength (σ_y > 100 ksi)

According to these, two series of alloys ; 18Cr-18Mn series, 18Cr-13Mn series, with different P and S impurity levels were prepared by Armco. In addition to the these four alloys, Armco's Nitronic 33 was also tested and evaluated for comparison.

Table A3   Alloy Chemistries

code	C	Cr	Mn	N	P	S	Ni	Si
23	.011	18.39	17.32	.54	<.005	.005	<.01	.11
24	.014	18.41	17.21	.55	.049	.014	<.01	.11
26	.012	16.99	12.25	.38	<.005	.008	<.01	.073
27	.011	17.06	12.30	.44	.041	.014	<.01	.075
Nitronic 33	.052	17.87	12.69	.30	.028	.007	3.42	.33

2. Specimens Preparation

As received (hot-rolled)

⟶ Cold (or Warm) rolled

⟶ Grain coarsening (1150 C, 15 hrs , Ar + N_2)

⟶ Annealed (1050 C, 10 min., Ar + N_2)

⟶ Aged (450 C, 700 C, 0 - 100 hrs)

Annealing at 1150 C for 15 hrs in the mixture of argon and nitrogen gas was determined to be the optimum condition to get 80-100 um grain diameter.

3. Testing and Results

Some important tests in this research are as follow.

- Pitting Corrosion Test ⎡ Potentiodynamic test

⎣ Immersion in ferric chloride solution

- SCC tests ⎡ Bent beam stress corrosion test

⎟ U – bend test

⎣ Slow strain rate test

- Precipitation study ⎡ metallography (optical, SEM and TEM)

⎟ X-ray diffraction

⎣ Thermal analysis

- Grain boundary chemistry ; SEM, EDS, TEM, STEM and AES analysis

3a. Pitting corrosion test

1) Potentiodynamic test   (ASTM Standard G5-82)

The specimens having different ageing treatment were studied by potentiodynamic test to find variations of passitivity and pitting potentials in 3.5% NaCl solution.
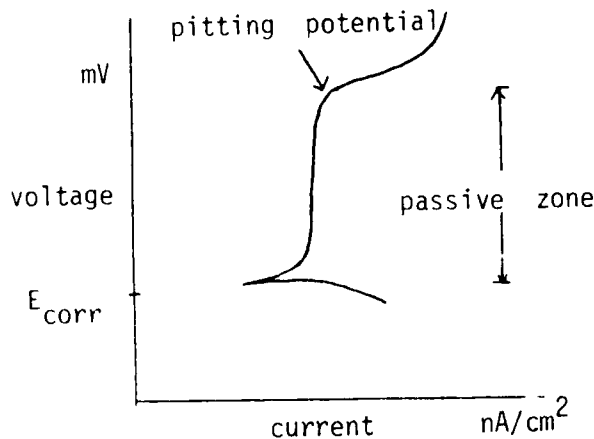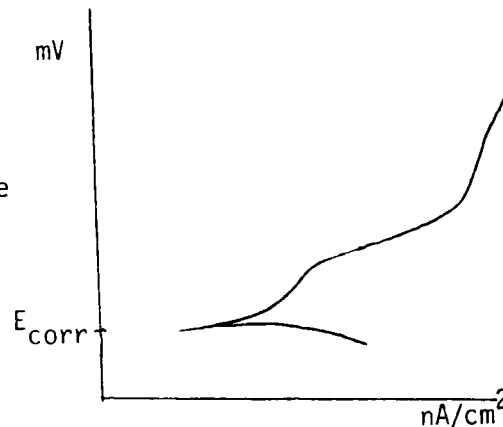

Fig. A II-a   Fig. A II-b

Two typical results were obtained. Specimens in the as quenched condition or with small amount of precipitate at the grain boundaries had the characteristics shown in Fig. A II-a. A distinct passive zone and high pitting potentials were observed (some did not show pitting).   The specimens with large amount of precipitates at the grain boundaries were very susceptible to pitting. (Fig.A II-b) Even with very careful specimen preparation , most of specimens could not avoid crevice corrosion at their edge sides because locallized pitting and crevice corrosion occured simultaneously.   Therefore, the relationship between pitting characteristics and the alloy chemistry could not be found. More detailed experiments will be done by optimizing the testing solution and the specimen geometry to avoid crevice corrosion.

2) Pitting test in ferric chloride solution

(ASTM Standard G 48-76)

Total immersion ferric chloride tests at room temperature were performed for all series of alloys. After 24, 48 and 72 hours exposure in the 6 wt. % $FeCl_3$ solution, the following results were obtained. For as-quenched specimens, the 18Cr-18Mn series is less susceptible to pitting than the 18Cr-13Mn series. For the specimens which were aged at 700 C for 12hrs and 48hrs, all specimens were severely damaged by pitting but Nitronic 33 showed the most resistance to pitting in this solution. In order to get good comparison among alloy chemistries, the concentration of testing solution, time for immersion and specimen geometry will be modified in the next series of measurements.

3b. Stress Corrosion Cracking (SCC) test

1) Bent-beam stress corrosion test

(ASTM Standards G 39-79, G 36-73)

Four points bending test in the boiling $MgCl_2$ solution has been aimed at trying to identify the transition of fracture morphology from the transgranuar mode to the intergranular mode in the sensitized specimens. Two welded specimens after quenching followed by annealing, showed transgranular cracking after exposure in this condition for one month. Two difficulties in this test are long time exposure, more than 4 weeks, and the localized pitting process which must be distinguished from the stress corrosion cracks.

2) U-bend test (ASTM Standard G 30-79)

Six specimens were tested in the 45% $MgCl_2$ boiling solution after being stressed in a U - bend configuration. The purpose of this test was to evaluate a boiling $MgCl_2$ solution as suitable corrosion media. The observation of the test results showed that the specimens (as-quenched) did not show any cracking even though severe pittings were observed after a 5 week exposure. This test will not be continued.

3) Slow strain rate test (ASTM STP 665)

For many alloy systems low tensile strain rates in the region between 10^{-4} and 10^{-6}/sec will promote SCC and serve as a screening test. This testing method willl be applied to our speccimens. Several acccessaries which attach to the electrohydraulic tension machine to perform the measurements are being designed and built.

4. Microstructure of the Carpenter's 18-18 Plus stainless steel

4a. Introduction

This work refers mainly to the microstructural observation of various phases formed in a Cr-Mn-N austenitic stainless steel. The occurrence of these phases varies upon the conditions of aging treatment such as temperature, time and cooling rate.

4b. Experimental Approaches

The heat treatments used in this investigation included annealing and aging. Materials were solutionized at 1000C for 3 hrs followed by water quenching, air cooling and furnace cooling to room temperature. Aging treatments consisted of heating at both 500 and 600C for times ranging from 4 hrs to 1000 hrs. The chemical composition of the 18Cr-18Mn stainless steel was as follows ; Fe-balance, Cr-18, Mn-18, Ni-0.4, Mo-1.0, C-0.1, N-0.45, Cu-1.0 Si-0.4, P-0.02, and S-0.009 in weight percent. The carbon content was higher than in the model systems.

weight percent.

4c. Microstructural observations

The modifications of microstructure in this material were made by successive precipitation reactions after aging treatments from solutionized condition at elevated temperature. Different cooling rates from the solutionizing heat treatment were found to affect initial precipitation reactions. However, as the holding time was increased, it was difficult to distinguish the effect of cooling rate.

Optical microscopy, SEM and TEM were used to investigate the microstructural changes upon aging. As a consequence of the aging treatment of 500C and 600C, the precipitation occured first a⁺ the grain boundaries and then on the twin boundaries. After a long holding time general precipitation occured in the grains. The precipitate along the grain boundaries turned out to be the discontinuous, lamellar precipitate as shown in Fig. A12-a.

Using the electon microscopy, the shape of grain boundary precipitates were determined to vary from blocky to plates to the form of lamellar precipitates.

The precipitation on twin boundaries extended to both sides of a twin parallel to coherent boundaries as elongated needles as shown in Fig. A.12-b. Although the widening of twin boundaries occurs by a continuous precipitation, no nodular or lamellar precipitation was observed at these locations. The fine, dot-like precipitates in the matrix were expected to form well-defined Widmanstatten arrays on further aging. The precipitation reaction after aging at both 500C and 600C was found to continue even after 1000 hr holding time with the reaction at 600C much more complete than at 500C.

Attempts were made with nickel-carbon double stage extraction replicas to identify the phases present. STEM with EDX microanalysis indicated that the precipitates both on the grain and twin boundaries as well as the lamellar precipitates contained Cr, Fe, Mo and very small amount of Si. The precipitates on the grain and twin boundaries were found to contain the relative amount of Cr-70%, Fe-22% and Mo-8% in average weight percent omitting the carbon. The indexing of electron diffraction patterns showed that the precipitate had the fcc $Cr_{23}C_6$ structure. Thus, it is appeared that the phase precipitating both on the grain and twin boundaries was a carbide of $(Cr,Fe,Mo)_{23}C_6$ type. No nitride was observed.

A20

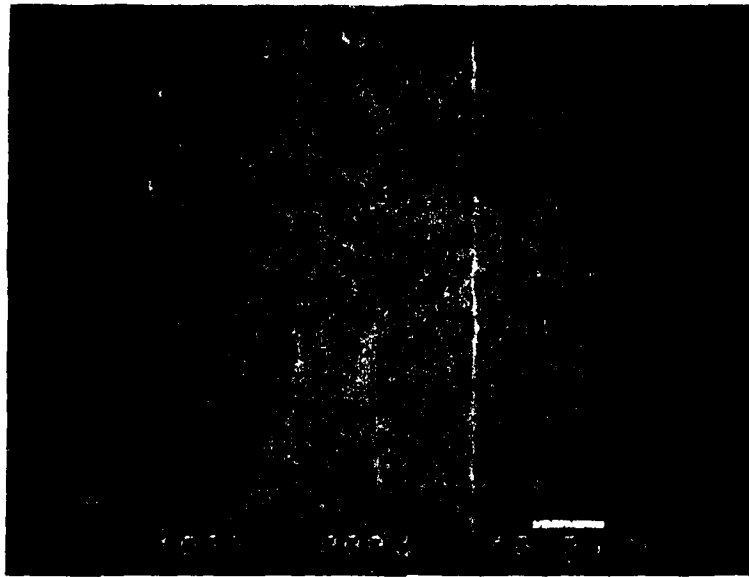Figure A.12-a   Scanning electron micrograph of a 1000 hr
                               aged specimen at 600C following
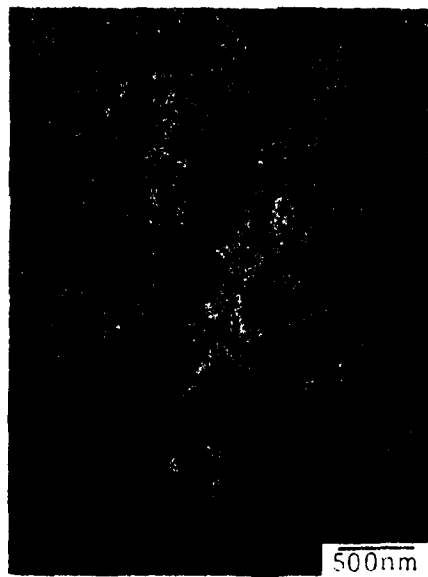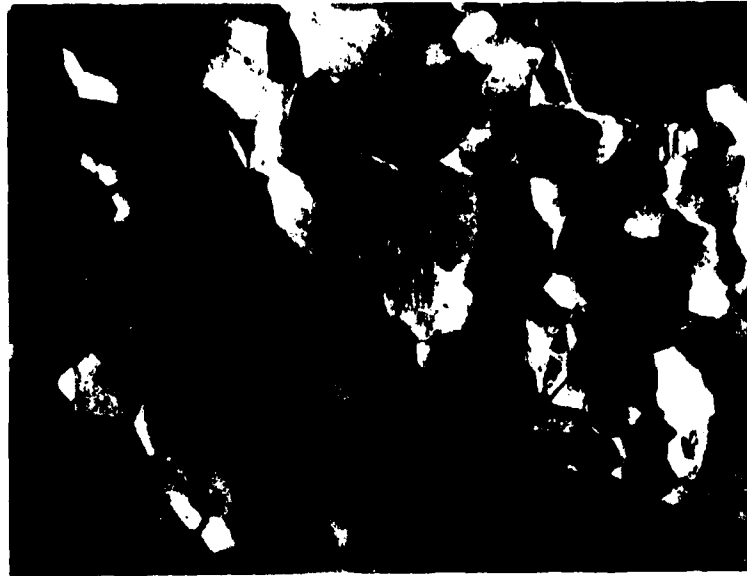   water-quenching

500nm

Figure A.12-b   Transmission electron micrograph of a 410 hr
                               aged specimen at 600C following
                               water-quenching

4d. Fracture Path Analysis

With an aid of SEM, the fracture surface was observed to be a mixed transgranular-intergranular mode with a higher fraction of intergranular fracture in aged specimens (256 hr and 1000 hr at 600C). The relative intergranular amount in the fractured region was much higher in a 1000hr - aged sample than that in a 256 hr - aged one. The former showed many facets which had dimples and roughness (Fig. A13-a), compared to the latter that has relatively smooth intergranular facets (Fig. A13-b).

Quantitative AES analysis was conducted for Fe, Cr, Mn, N, C, P, O, Ni, Mo, Cu, Si and S by comparison with standard peaks. There appears to be a depletion of Cr and N on the fracture surface of aged specimens with respect to the solutionized sample. The AES spectra taken from the aged specimens showed P peak (Fig. A14) indicating segregation of the P during the heat treatments. The quantitative data showed an increase in P on the fracture surface for the 256 hr aging, but was reduced for the 1000 hr aging treatment. The change in fracture mode described earlier might mean a reduction in true grain boundary fracture explaining the lower P content.

As an attempt to investigate the nature of the lamellar precipitates along the grain boundaries, Auger line scanning was performed across a huge lamellar precipitate along the grain boundary. The relative peak heights of C and Cr increased noticeably and the Fe peak droped sharply inside the area of lamellar precipitate. The N peak did not change much. This supports the finding that precipitate is a carbide.

(a) 1000 hr aged one
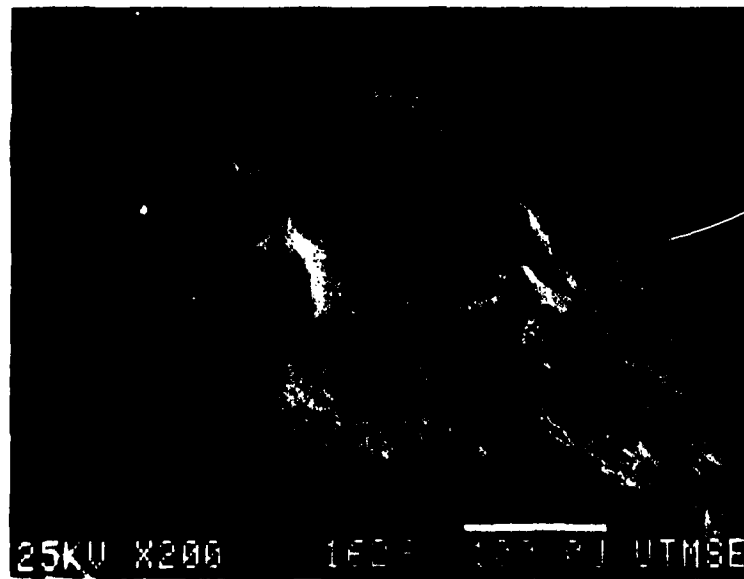
(b) 256 hr aged one

Figure A.13   Scanning electron fractrographs of aged
               specimens at 600C following
               water–quenching

A23

UT MS & E

$\dfrac{dN}{dE}$

Electron Energy eV

SPECIMEN

	1003WC-660-256		PEEPAK
E_p 5KV	I_p 16uA		
Vmod 3	Vmult 1000 V		
RC 0.1/5	SENS 10 X		
DATE	BY		
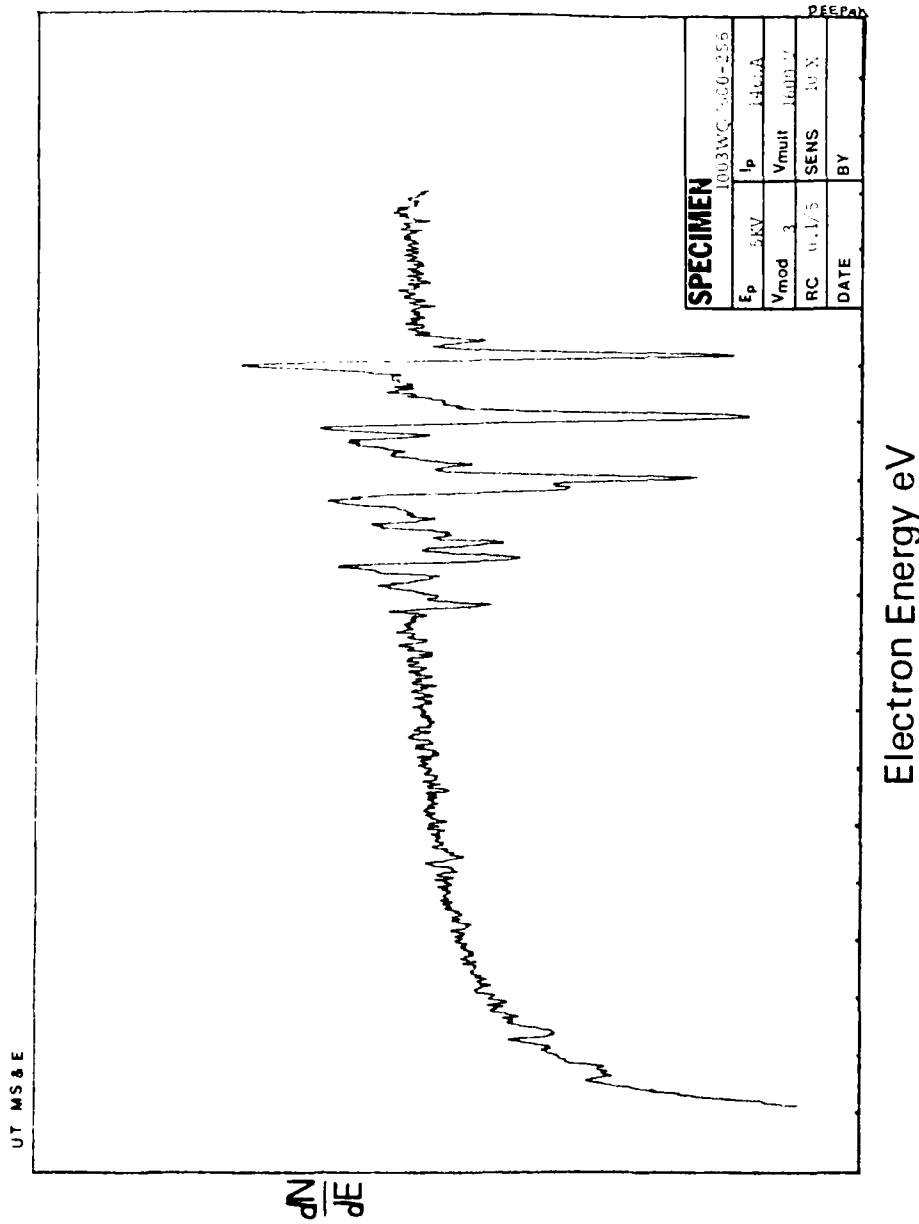
Figure A.14   Auger spectra of a 256 hr aged specimen
at 600C following water-quenching

Reference

A1. E. V. Barrera, Thesis, The University of Texas at Austin (1984).

A2. D. Y. Lee, E. V. Barrera, J. P. Stark, and H. L. Marcus, " The Influence of Alloying Elements on Impurity Induced Grain Boundary Embrittlement Met Trans A, vol 15A, no 7, July 1984, pp. 1415-1430.

A3. D. Y. Lee, Dissertation, The University of Texas at Austin (1983).

A4. G. J. Theus and R. W. Staehle, " Review of SCC and HE in austenitic Fe- Cr-Ni alloys," SCC and HE of Iron base alloys, NACE p. 845, 1973.

A5. V. Cihal and P. Pohoril, " Austenitic Cr-Mn steels resistent to SCC in the concentrated chloride solutions," Ibid. p.1170, 1973.

Appendix B

Introduction

In this appendix, the study of the failure of a model of layered systems (B1) is extended to include Ni-Ni and Ni-NiO-Ni systems. These systems have been chosen since nickel is a structural material as well as it being an important addition to many other alloy systems. Nickel also was chosen because there would be less complications due to the formation of its natural oxide. NiO is an important oxide system in electronic packaging and the selection of NiO gives one the opportunity to study the transition metal oxides and their related electronic switching properties. The experimental methods are much the same as those for the $Al-Al_2O_3-$ Al- Graphite system (B1). Specimen preparation involved vapor deposition and diffusional oxide formation. Specimens were tested in tension at room temperature. AES analysis was performed before and after fracture testing . Electronic switching charactistics were checked prior to fracture testing. The present emphasis was placed on obtaining reproduceable mechanical testing data as well as reproduceable switching. All the above will be described in more detail in the following sections.

Material Description

Each specimen is made up of two parts; the substrate material which is either in the unoxidized or oxidized state and the vapor deposited film which ranges in thicknesses from 100 Å to 3500 Å. The Ni substrate is cut from a polycrystalline rod 99.99% pure with an average grain size of 50 μm. Preparation of the substrate involves polishing one surface using 0.05 μm alumina and lightly etching the surface in a mild HCl-methanol solution. Oxidized specimens can then be made when requir-

sufficient momentum transfer with a well defined stress wave.

Experiments, using silicon substrate-aluminum film specimens, have shown qualitative success for film detachment. The magnitude of the shock wave was not determined in this preliminary work. The laser spallation method has shown, for metal-metal film adhesion, a direct correlation of the threshold power with the calculated metal-metal interface bonding strength.[C18]

These investigations have indicated some inovative methods of studying and improving the integrity of aluminum-graphite interface in these metal matrix composites. This effort will continue under DARPA/ONR contract*: ONR N-00014-84-K-0687.

a minimum of one gram full scale load has been obtained. Fig. C6 represents the results of the quantitive strength change measurements. The large error bar for the fracture strength of single crystal graphite was partially due to the lack of a distinct fracture area.

As discussed previously, switching was not observed with the oxides in this study. Failure, however, did occur at the oxide-grahpite interface. This is consistent with failure in the high conductivity state of earlier studies.[C5] Failure was brittle in all cases. Failure aspects were not investigated for the N-type switching structures.

Our present work has produced suggestive evidence of the causal relationship between electrical and fracture characteristics. A bluish appearance of the graphite fracture surface was observed after interfacial failure in the high conductive state. Subsequent AES indicated no oxide present on this surface eliminating refraction from thin layers as a possible cause. The bluish color change has been observed in intercalation studies of single crystal graphite and is associated with the reduction of the graphite(i.e. electron deficient).[C14] This viewed in the context of the previously discussed catalytic effect of the aluminum oxide on grapnite presents some interesting possibilities. There are also published calculations of metal island shape changes in cermet structures due to electrical field effects on the island's surface energy.[C15] This suggest that strain effects merit further investigation.

The inherent difficulties of the DPO method may be circumvented by utilizing the laser spallation method of adhesion measurement.[C16] In laser spallation, a thin film is detached from the substrate without any prior disturbance of the film by impinging a pulsed high energy laser beam onto the back side of the substrate. The shock wave produced in the substrate, due to localized substrate melting, is used to stress the substrate-film interface. By increasing the incident laser power, one can find a threshold at which the film is torn loose from the substrate. AES is then used to determine the fracture path. From this data, it is possible to qualitatively measure film-substrate bond strength. The system may be made quantitative by measuring shock wave intensity with a quartz stress guage for various values of laser power and substrate thicknesses.[C17]

The intensity of the shock wave across the substrate-film interface requires the use of a grid of small thin film dots. The dots either adhere to the substrate or are totally removed when stressed by the laser. In addition, due largely to the substrate melting temperature, a polymeric or metal film may be required on the backside of the substrate to initiate

reactive method of evaporation used in that study produced a cermet structure consisting of aluminum islands in an amorphous oxide matrix. The structures only switch in a critical range of aluminum island concentration, but show high conductivity at greater aluminum concentrations and low conductivity at lower aluminum concentrations.

While the states of switching may be associated with percolation theory,[C13] the onset of switching may be related to the impurity level in the amorphous oxide matrix. Once conduction is initiated via impurity levels in the band gap, the negative thermal coefficient of resistance of the amorphous matrix will produce Joule heating promoting some type of transformation to high conducting short circuit filments. Return of the low conductivity state after a period time may be related to ion diffusion.

The high state of conductivity observed in our evaporated oxide films have resulted either from a very high impurity concentration or from a deviation of oxide stoichiometry. Auger spectroscopy indicates that the former is unlikely. However, when our oxygen-to-aluminum peak height ratios were compared to those of Tsai's[C2] a large difference was observed. There was an increase from 1.4/1.0, in Tsai's switching composites, to 4.7/1.0 in our conducting composites. The ratios were measured by comparing respective peak-to-peak heights at maximum oxygen signal in AES sputter profiles through the respective oxides. The measured ratio of oxide composition for our oxides does not agree with the previously discussed EELS data. However, approximations used in both EELS and AES may contribute to this discrepency. If excess oxygen was present in our oxides, the off-stoichiometric proportions of cations and anions would create a greater concentration of charge carriers permitting the high electrical conductivity state.

3.3-Strength Measurements

Whereas previous mechanical methods of strength testing were qualitative,[C5] in the current study an attempt was made to quantify strength changes of the switching model composite structures. The direct pull off (DPO) method was used. Fig. C5 is a schematic of the set-up. Certain difficulties with alignment and mixed tensile-shear loading are inherent with this method, but its relative simplicity makes it useful. Failure loads encountered were between two and thirteen grams, but resolution was limited because equipment availability restricted the minumum full scale load to 450 grams. For future work, a load cell having

This is roughly consistent with studies on anodically prepared aluminum oxide thin films(i.e. 50 nm).[C8] Both our amorphous oxides and the anodic ones transformed to 10 nm crystallites of gamma-Al_2O_3 when heated sufficiently by the electron beam. Preliminary observations made in this study showed little preferred orientation to the single crystal graphite substrate during crystallization. Representative EELS spectra and TEM micrographs are shown in Fig. C1 and Fig. C2.

3.2-Electrical Characterisitcs

The electrical characteristics of the reactively evaporated films where ohmic with high conductivity. Characteristics of the earlier switching was only observed at random spots and was not reproducible from specimen to specimen. The resistivity of these films was calculated to be in the range of 10^6 ohm-cm. In comparison, published values of anodic thin films of Al_2O_3 vary from 10^{12} to 10^{17} ohm-cm.[C9]

In contrast to the reactively evaporated films and films of earlier studies, the thermally oxidized films showed stable reproducible switching of a different type. An experimental I-V trace is shown in Fig. C3. The switching observed in the thermal oxides is known as voltage controlled N-type switching. The switching observed in earlier reactively evaporated oxides is known as bistable memory switching. Another type of switching which has been reported in literature is known as current controlled S-type switching.[C10] Schematic representations of the three types are shown Fig. C4. The bistable memory switching may be indistinguishable from the S-type switching under constant voltage testing since the negative resistance region will not be observed. However, persistence of the high conductivity state(i.e. memory) would be an indication of the bistable switching.

The negative resistance region in the N-type switching has been attributed to impurity levels in amorphous insulator band gaps.[C10] Anodic aluminum oxide films also exhibit the N-type switching.[C10] The hydrocarbon content in the welding grade oxygen used for our thermally grown oxides is the most probable impurity source.

For bistable memory switching, conduction has been attributed to the formation and burn-out of microfilaments in a generally amorphous insulator thin film.[C11] Recently, this type of switching has been observed in reactively evaporated aluminum oxide films.[C12] The

chamber where the diffusion pump was liquid nitrogen trapped. This was hoped to reduce the hydrocarbon contamination. Future work will incorporate an all metal ultra-high vacuum chamber. The oxide was deposited at rates less than 0.5 nm/sec in the O_2 atmosphere at a vacuum of 10^{-4} Torr. The aluminum overlayer was deposited at rates greater than 2.0 nm/sec in a vacuum of 10^{-6} Torr. The substrate was Ticonderoga single crystal graphite having a [0001] surface normal. The substrates were sandwiched between a tantalum mask. Oxide thicknesses averaged 25 nm while the aluminum layers averaged 100 nm. Deposition rates and thickness were measured by a quartz crystal oscillator. The source-to-substrate distance was approximately 11 cm. Heat flux from the source produced a temperature rise of less than 10^0C at the mask. In addition to reactively evaporated oxides, some aluminum oxides were produced by depositing aluminum on the substrates and resistivly heating the tantalum mask in an atmosphere of welding grade oxygen at a pressure of 10^{-4} Torr. The hydrocarbon content of the welding grade oxygen was unknown.

Tungsten electrical probes, used in earlier studies[C5], showed spurious contact effects in this study. A switch to tungsten probes vapor coated with gold then dipped in mercury produced stable ohmic contact. A Tektron I-V curve tracer was used to measure electrical characteristics of the layered composites. The unit provides voltage controlled measurements at 120 Hz. The unit is generally used to determine diode and triode current-voltage characteristics.

3--Results and Discussion

3.1-Structural

It is well known that reactive evaporation produces film structures ranging from amorphous to pure metal-reactive compound mixtures depending on deposition rate and background pressure.[C7] By depositing the oxide film on transmission electron transparent single crystal graphite the film structure was studied. This was done for all specimens except those made by thermal oxidation. In every case the oxide film was amorphous as determined by electron diffraction. The presence of aluminum and oxygen was verified by electron energy loss spectroscopy (EELS). Preliminary results of a semiquantitative analysis of the EELS spectra showed that the oxide's composition was in the ratio of Al_2O.

likely candidates are halides of metals such as Pb, As, S, and Fe. To study this hypothisis a set of experiments will be carried out. A suitable graphite substrate will be treated with the metal halide and then coated with aluminum oxide and aluminum metal. These samples will be heat treated at various temperatures and for varying times then studied by use of analytical electron microscopy.

1.2- Oxide Switching

Tsai[C4] and Mendez, et.al [C5] have observed a phenomena of correlation between the electrical and the failure characteristics of $Al/Al_2O_3/Graphite$ planar composites used to model the interface of aluminum /graphite metal matrix composites. When the sandwiched aluminum oxide layer is in a low electrical conductivity state, failure occurs through the oxide. This has been thought to be an indication of a high strength bond at the oxide-graphite interface. Failure may be switched to the oxide-graphite interface by voltage switching the oxide layer to a high electrical conductivity state. This failure mode has been associated with a lower bonding strength at the interface. These characteristics are reversible in that after a period of time the oxide returns to its low conductivity state and when stressed, failure occurs through the oxide. The oxide layer was identified by Lo as gamma-Al_2O_3 [C6]

These earlier investigations utilized vacuum systems where the diffusion pump was not liquid nitrogen trapped. The vacuum used during reactive evaporation of the switching oxides was 10^{-4} Torr. Backstreaming from the diffusion pump would place a large percentage of hydrocarbons in the chamber atmosphere at this vacuum. The effect of this impurity on the oxide-graphite's interfacial properties as well as the oxide's electrical properties is unknown. In addition, measurements of interfacial strength changes due to conductivity state changes were only qualitative being limited to fracture path determination. The research in this report was aimed at cleaning up the reactive atmosphere, verifying the structural characteristics of the evaporated oxide film, and making a quantitative measure of strength changes in the planar composites.

2-Experimental Procedure

High purity oxygen was used as the reactive atmosphere in a vacuum

Appendix C

Interface Failure in Al/Graphite MMC

1-Introduction

A potential source for material meeting the stringent requirements
of some aerospace and military designs has been the metal matrix
composites(MMC). These materials are tailored to provide optimum
properties for specific applications. However, there is a weak link in the
structure which produces these properties. The interface between the two
components that make up the composite results in a complex reaction
zone that limits or degrades the MMC's properties. The primary purpose of
the present investigation is to use some inovative methods to characterize
and to strengthen the interface of aluminum/graphite composites thereby
broadening its potential use.

1.1-Al/Graphite Reactions

Earlier investigations have shown that a layered model of
aluminum/aluminum oxide/graphite has simplified and provided insight
about the nature of the aluminum/graphite interface.[C1] Al/Graphite
composites, when heat treated in a moderate vacuum, form a carbide at
the interface between the aluminum metal and aluminum oxide.[C2] This
carbide forms in non-uniform manner becoming a site for stress
concentrations which severely diminish the longitudinal strength of the
composite. The conditions under which the carbide will grow have been
characterized. However, as of yet, neither the formation process nor any
means of suppressing the formation have not been studied in detail.
The key to understanding the carbide formation process lies in
realizing the role of the intermediate oxide layer as a catalyst in the
decomposition of the fiber. In other words, the fiber can be thought of as
a completely dehydrogenated polymer which is "cracked" by the oxide
catalyst as is the case with many catalytic cracking processes.[C3]
Suppressing the carbide formation then becomes a problem of
poisoning the catalyst. Drawing from the science of catalysis, the most

B4. N. Fuschillo, B. Lalevic, and B. Leug," High-Field Transport in NiO and $Ni_{1-x}Li_{1-x}O$ Films," Solid-State Electronics, vol 19, Pergamon Press, 1976, pp. 209-219.

ELEMENT		Etching
1	0	2	E_p 3 Kv
2	Ni	1	I_e 25 mA
3	Cl	5	
4	C	5	2.5/Div

SPECIMEN Ni-NiO-Ni

Cl

0

Ni

PEAK TO PEAK HEIGHT

Ni

0

C

Cl

Spec. no. 1   Spec. no. 2

Time   min/div

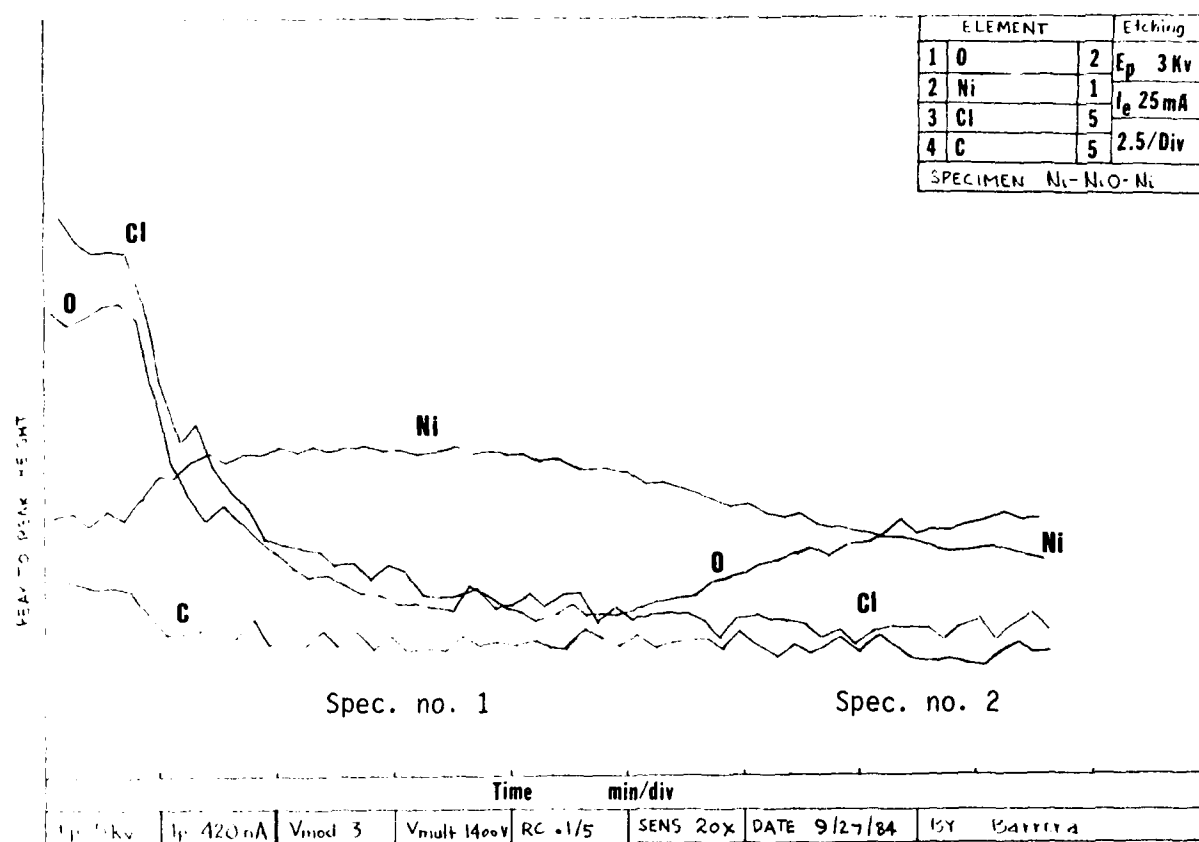| E_p Kv | I_p 420 nA | V_{mod} 3 | V_{mult} 1400V | RC .1/5 | SENS 20x | DATE 9/27/84 | BY Barrera |

Figure B.5. Sputter profile of a deposited Ni-diffusion formed Ni oxide-Ni
substrate specimen. X indicates point at which sputtering
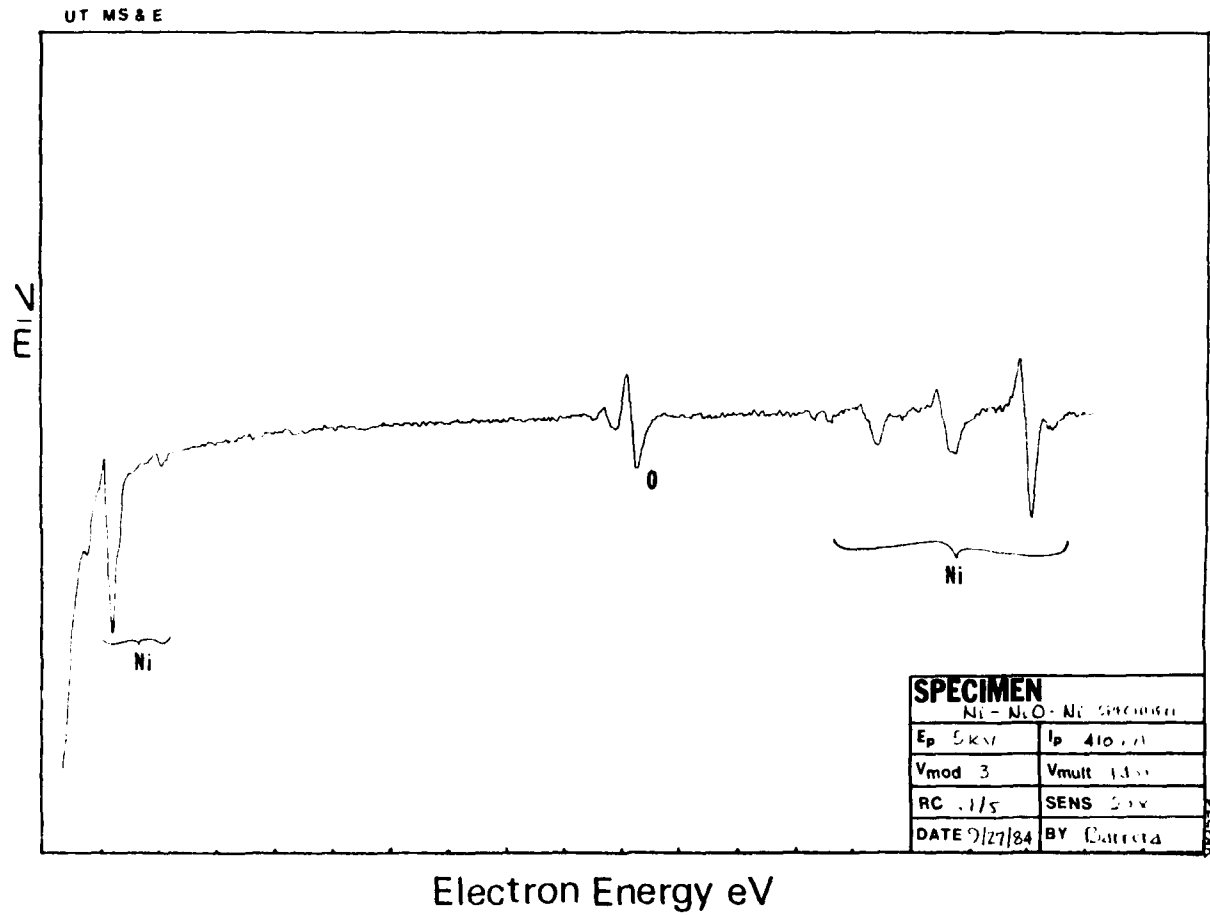started. The substrate Ni was not sputtered.

Figure B.4. Spectra no. 2 is an Auger select point analysis of the diffusion
formed Ni oxide. The point at which the spectra was taken is
indicated on the sputtering profile enclosen in this appendix.
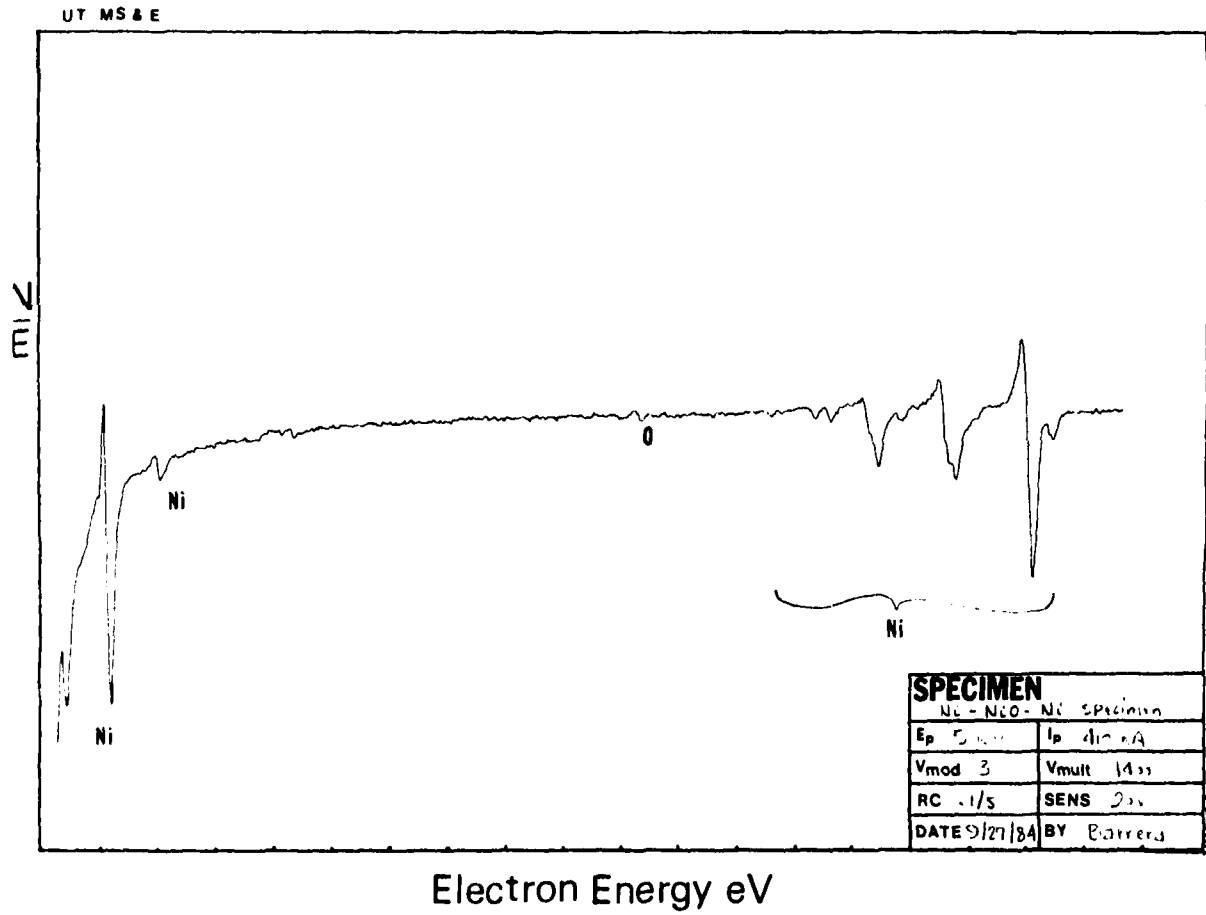
Figure B.3. Spectra no. 1 is a Auger select point analysis of the deposited Ni thin film. The point at which the spectra was taken is indicated on the sputtering profile enclosed in this appendix.

in Figures B.3-B.5.

The results seem to indicate that switching can only be observed when oxide thicknesses exceed 1.0 μm. A majority of the references on NiO switching (B2-B4) seem to confirm this. However it is expected that the thinner film are not uniform and continuous and are not in a condition for switching to occur. Since this research is concerned with very thin interfaces (monolayers and up to 100 Å), switching may not be relatively important in this system.

Fracture of the Ni-Ni specimen has been observed yet it has not been determined by means of AES whether the fracture occurs at the interface or in the deposited Ni film.

References

B1. H. L. Marcus," Microscopic Study of the Influence of Impurities on Interface Bonding," UTCMSE-84-1 Annual Technical Report-Office of Naval Research Contract N00014-83-K-0143, Jan 25, 1984.

B2. J. F. Gibbons and W. E. Beadle," Switching Properties of Thin Ni-O Films," Solid-State Electronics, vol 7, Pergamon Press, 1964, pp. 785-797.

B3. N. Fuschillo, B. Lalevic, and B. Leug," Electrical Conduction and Dielectric Breakdown in Crystalline NiO and NiO(Li) Films," Jl of Applied Physics, vol 46, no 1, Jan 1975. pp. 310-316.
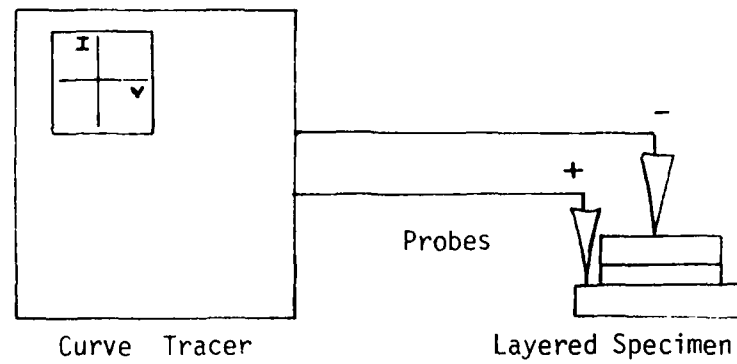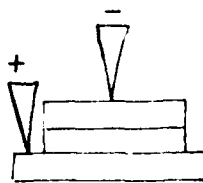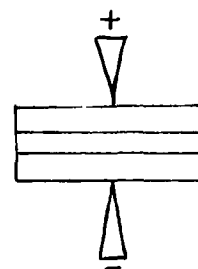
Figure B.1. Diagram of IV Test Setup showing the curve tracer and point contact probes setup on specimen.

(a)

(b)

Figure B.2. Two probe setups are in use as shown. Probes are made of either tungsten or gallium- indium coated indium.

ed by heating the specimen in a tube furnance for a pre-determined time. The specimen is then lightly polished and etched prior to deposition. The deposited Ni thin films are made in a $1x10^{-6}$ torr vacuum from a 99.999% pure Ni filament wire. Thicknesses are monitored by a thickness monitor and checked with a thickness profilometer.

Experimental Approach

After the specimens are made, their switching characteristics are checked as shown in Figures B.1 and B.2. Mechanical testing, using a 500 N load cell was done on an Instron Universial Testing Machine. Select point Auger analysis as well as argon sputtering profiles were obtained from various specimens. Fractographs of the fractured surface were used in the determination of the size of the fracture surface area.

Results and Discussion

At this time electronic switching of the Ni-NiO specimens is hard to characterize and is not considered very reproduceable. Switching was not observed in the Ni-Ni specimens where a natural oxide was present at the interface. Specimens with deposited films with thicknesses less than 1.0 µm did not show signs of switching.

Mechanical testing of the adhesive which connects the specimen to the testing apparatus was extensively done and proved to be quite reproduceable. Mechanical testing of the Ni-Ni interface and the Ni-NiO-Ni specimens is now underway.

Examples of Auger select point spectra and sputter profiles are shown

REFERENCES

C1.   Marcus,H.L.,Final Technical Report UTMSE-83-1,(1983),ONR Contract
       N00014-78-C-0094.

C2.   Finello,D.,Ph.D. Thesis(1982),The University of Texas,Austin,Texas.

C3.   Rase,F.,Chemical Reactor Design For Process Plants,John Wiley &
       Sons,New York,Vol. 1,pp. 97-99.

C4.   Tsai,S.D.,Ph.D. Thesis(1980),The University of Texas,Austin,Texas.

C5.   Mendez,H.,Finello,D.,Walser,R.,Marcus,H.L.,Scripta Met.,16(1982),
       pp. 855-858.

C6.   Lo,J.,M.S. Thesis(1981),The University of Texas,Austin,Texas.

C7.   Maissel,L.,Glange,R.,Handbook of Thin Film Technology,McGraw-Hill,
       New York,(1970),pp. 145-160.

C8.   Bourdillon,A.J.,El-Mashri,S.M.,Forty,A.J.,Phil. Mag. A,49-3(1984),
       pp. 341-352.

C9.   Gitzen,W.H.,Alumina Ceramics,(1976),AFMRL-TR-66-13,p. 156.

C10.   Chopra,K.L.,Physics of Electronic Ceramics,(L.L. Hench,D.B. Dove ed.),
       Marcel Dekker,Inc.,New York,(1971),pp. 283-311.

C11.   Silva,D.O.,Dir,G.,Griffiths,C.,J. Non-Cryst. Solids,2(1970),
       pp. 316-333.

C12.   Demiryont,H.,Tezey,N.,Thin Solid Films,101(1983),pp. 345-356.

C13.   Coutts,T.J.,Thin Solid Films,38(1976),pp. 313-321.

C14.   Samorgai,C.,(a private communication).

C15.   Milgram,H.A.,Lu,C.S.,J. Appl. Phys.,39-3(1968),pp. 1624-1628.

C16. Vossen,J.L.,ASTM STP 640,(K.L. Mittel ed.),American Society for Testing and Materials,1978,pp. 122-133.

C17. Graham,R.A.,Neilson,F.W.,Benedick,W.B.,J. Appl. Phys.,36(1965), p. 1775.

C18.. Buckley,D.H.,Wear,20(1972),pp. 89-103.

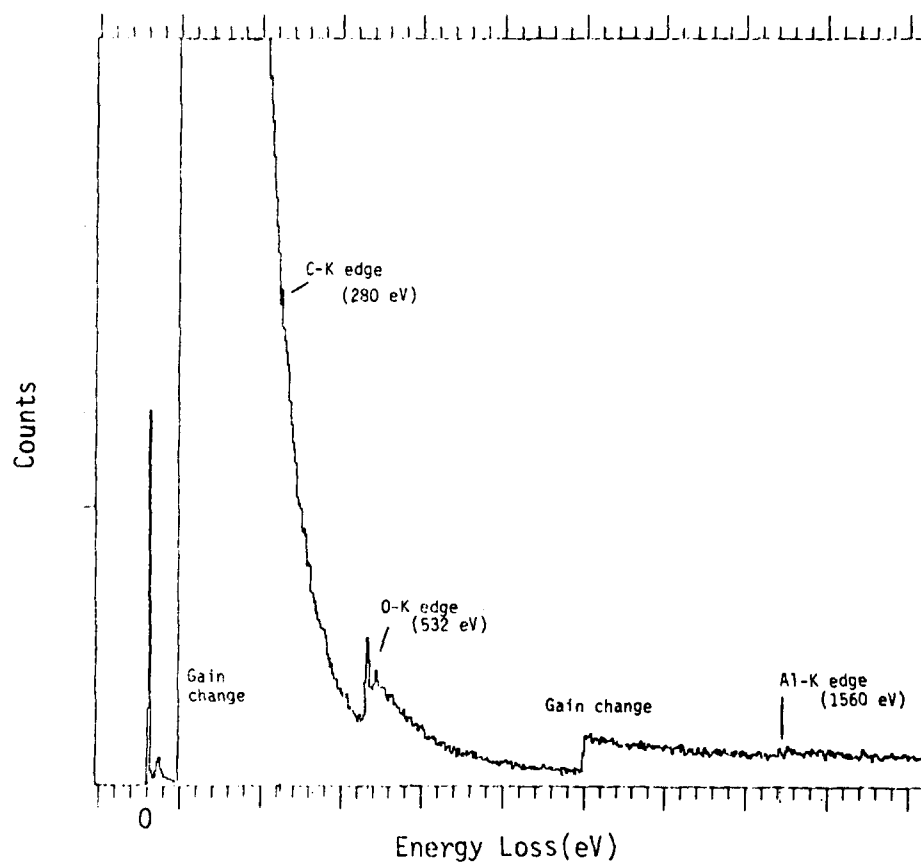Fig. C1 Electron Energy Loss Spectrum for the reactively
evaporated amorphous aluminum oxide observed in this
study.

53

ONR-1984, C 11
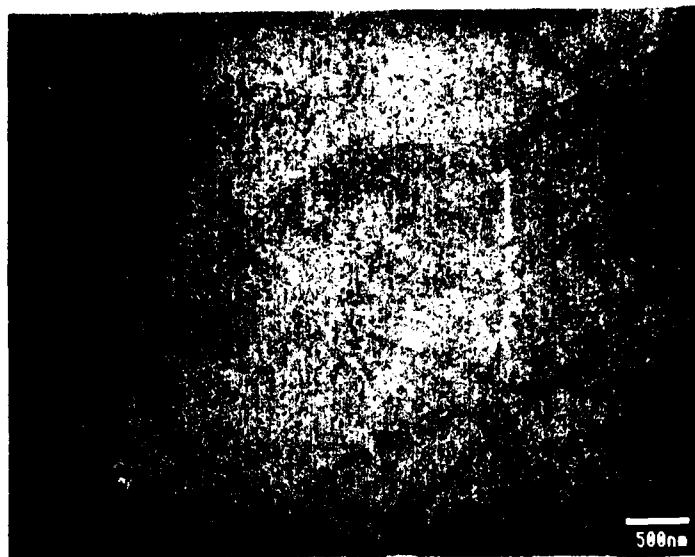
(a)

(b)   (c)

Fig. C2 Electron beam damaged area of amorphous aluminum oxide
         on (0001) oriented single crystal graphite.

         (a) Bright field image of crystallites
         (b) Electron diffraction of partially crystallized
             amorphous oxide
         (c) Electron diffraction of fully crystallized
             oxide(gamma-Al_2O_3)
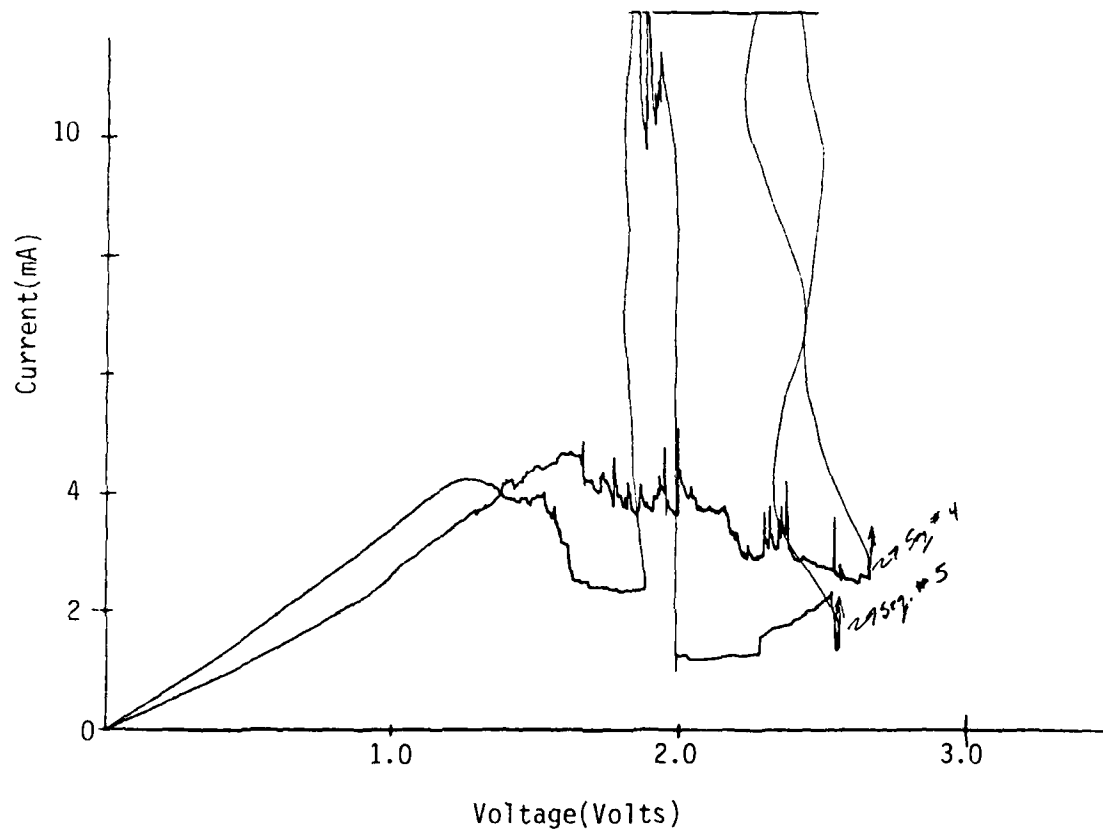
Fig. C3 Voltage-Current characteristics of switching thermal oxides observed in this study

Fig. C4   The three switching characteristics of amorphous
           oxides: (a) voltage controlled N-type,(b) current
           controlled S-type,(c) bistable memory

Fig. C5   Schematic of the apparatus used in the DPO method of mechanical testing.

Fig. C6   Preliminary measure of the strength
change in the switching composites
referenced with graphite crystal
strength

Appendix D

ELASTIC CONSTANTS VERSUS MELTING TEMPERATURE IN METALS

M.E. Fine*, L.D. Brown and H.L. Marcus
Center For Materials Science and Engineering and
Dept. of Mechanical Engineering, The University of Texas, Austin, TX 78712
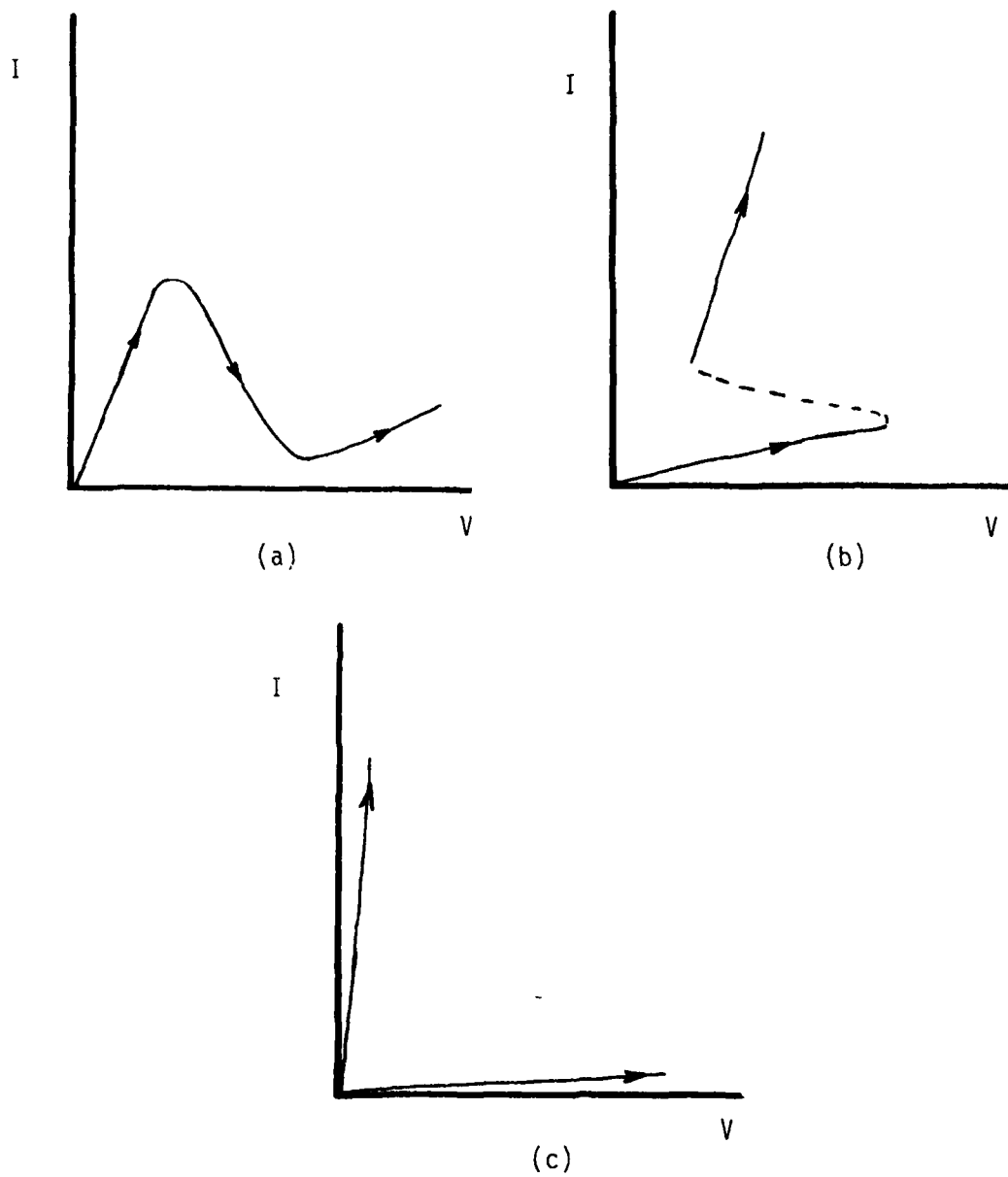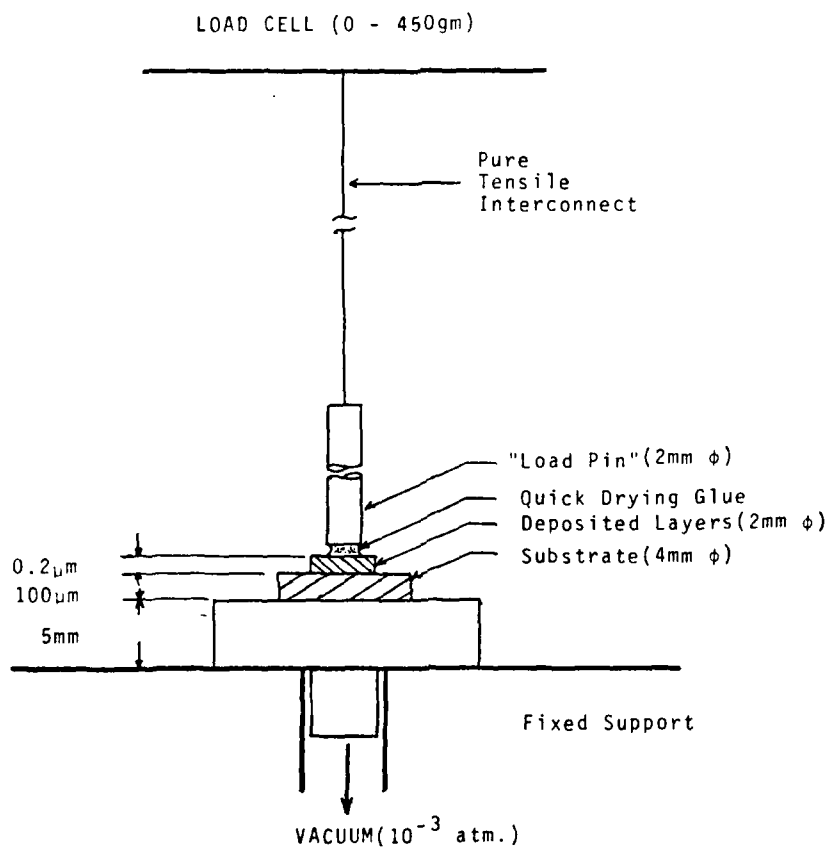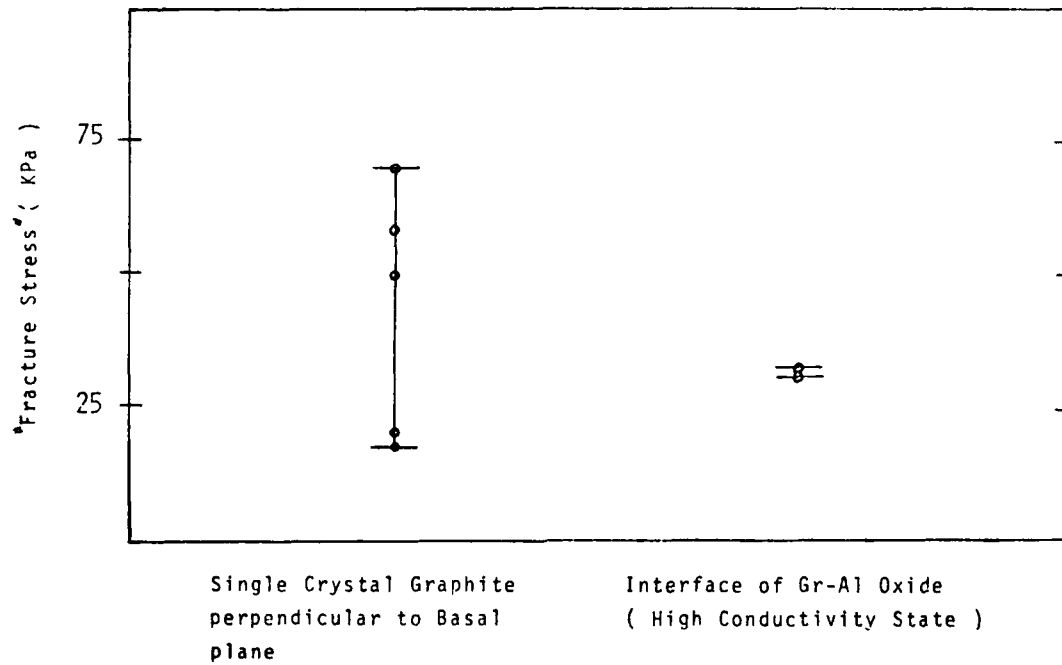
Rapid solidification techniques significantly broaden the possibility for developing dispersion strengthened alloys where the dispersed phase is in thermodynamic equilibrium with the matrix. The extent of solubility is much greater in the liquid state. Rapid solidification leads to extended metastable solid solubility or to second phase crystallites less than 1 um in size, an excellent size for dispersion strengthening. With extended solubility an aging treatment is able to develop a larger volume fraction of dispersed phase than by the usual solution treatment. The new elevated temperature alloy, Al-8 wt % Fe - 3.5 wt % Ce, (1) is an example of a new alloy made possible by rapid solidification.

In selecting intermetallics for possible RSP dispersion strengthened alloys, increased elastic modulus is often a major objective, but unfortunately little information on the elastic constants or moduli of intermetallics is available. As is well known from examination of tables of elastic constants of metals, there is a rough correlation between modulus and melting temperature. Tungsten which has the highest melting temperature has the highest elastic constants for cubic metals while Na which has a low melting temperature has very low values of the elastic constants.

The present note examines the empirical relationships between the elastic constants and the melting temperature in more detail to determine the extent to which it may be used for predictive purposes. For high temperature alloys low values of solubility limits are important to achieve low particle coarsening rates. Much data on solubility limits and melting temperatures are available from published phase diagrams.

Figure 1 is a plot of room temperature C_{11} for cubic metals and intermetallic compounds. The number by each point refers to Table I which identifies the metal or compound and gives the reference for the data. Only data for compounds which persist to their melting temperature are included. The elastic constant data was obtained for the most part from the compilation of single crystal elastic constants published by Simmons and Wang (2). These were supplemented by results for additional metals not contained in this compilation. The melting data were obtained from the Hansen-Shunk-Elliott or the General Electric Co. phase diagram volumes. The correlation for the 19 metals and 27 intermetallic compounds is rather good. A least squares best fit straight line obtained from the data with C_{11} in GPa and T_m in deg. K is $T_m = 553 + 5.91C_{11}$. The determination coefficient is 0.87. This equation is shown by the solid line in Fig. 1. The dashed lines represent a confidence level of +/- one standard error of estimate.

The data for Th and Ta represents the worst deviation from the best fit line. As subsequently discussed the lanthanides do not follow a correlation of $(2C_{11}+C_{33})/3$ with T_m. Thorium being an actinide falls into this same category. As with the lanthanides for the best fit line in Fig. 4, the Th datum point was not used in determining the least squares line in Fig. 1. Another factor is that Th transforms from the BCC to FCC structure at 1400°C prior to melting. Thus the structure which melts is not the one present at room temperature corresponding to the measured elastic constants.

The predicted C_{11} values for Ta and Nb are noticeably higher than the measured values. It is perhaps worthwhile to point out that Ta and Nb have opposite signed anisotropy factors from other cubic metals. The intermetallic compound points lie closer to the line than the

Permanent address: Dept. of Mat. Sci. and Eng., Northwestern University, Evanston, IL 60201.

elemental metals. The coefficient of determination for the intermetallic compounds alone is 0.90 while r^2 for the elemental metals alone is 0.82.

The bulk modulus ($B=(C_{11}+2C_{12})/3$ is plotted for the same metals and intermetallic compounds in Fig. 2. The spread among the data set from the best fit straight line, $T_m= 607 + 9.3B$ is greater than for C_{11}. This derives from the fact that C_{12} does not correlate at all well with melting temperature.

Since covalent bonding dominates in diamond cubic and GaAs structured semiconductor materials C_{11} vs T_m are examined for these separately in Fig. 3 (Table II). The least squares best fit line drawn on Fig. 3 is $T_m= 412 + 8.2C_{11}$ with a determination coefficient of 0.71. Thus T_m is not as good for predicting C_{11} of III-V semiconductor compounds as for metallic intermetallic compounds. Interestingly with C_{11} of diamond equal to 1075(3) GPa, a melting temperature of 9227°K is predicted.

Finally some data for hexagonal and tetragonal metals and intermetallics are plotted in Fig. 4. Here $(2C_{11} + C_{33})/3$, that is $\bar{C}_{ii}$, values are plotted versus T_m.

As discussed below the lanthanides and groups 3b and 4b elements are far off the distributions. The first 18 data points of Table 4, which do not include any of these elements as well as Be and Tl which undergo phase transformations, are plotted as closed and open circles in Fig. 4 (Table III). The least square straight line through this data set, $T_m= 354 + 4.5\bar{C}_{ii}$, is plotted. The coefficient of determination is 0.94 indicating useful predictive relationship. Data for eight lanthanides are plotted as squares, all of these lie considerably above the best fit line plotted on the figure neglecting these data. It is noteworthy that T_m increases with number of 4f electrons with little increase in $\bar{C}_{ii}$. All of these metals transform from HCP to BCC before melting as do Be and Tl which however lie close to the best fit line even though their data points were not used to establish the line. The datum point for Co was used even though it transforms because the coordination number remains constant.

The group 3b and 4b metals, plotted as open squares in Fig. 4 also do not fit the correlation. Their $\bar{C}_{ii}$ values lie substantially on the low side of the $\bar{C}_{ii}$ vs T_m established by not including these data or the data for the lanthanides. Again all undergo phase transformation before melting. Compounds containing these metals do fit the correlations in Figs. 1 and 4 rather well, however.

Cerium, the first of the lanthanides, is FCC at room temperature in contrast to the others in the series. Its C_{11} at room temperature is 26 GPa (29) which is very low considering its T_m of 970°K. It thus falls in the same classification of the other lanthanides in this respect.

Conclusions

The correlations presented show that melting temperature may be used for preliminary estimation of the C_{11} elastic constant in cubic intermetallic compounds. The estimation also holds for estimating $\bar{C}_{ii}$ in hexagonal or tetragonal intermetallics where $\bar{C}_{ii}$ is $(2C_{11}+C_{33})/3$. The elemental metals in groups 3b and 4b as well as the lanthanides and actinides do not follow the correlation. The C_{12} constant and bulk modulus do not correlate well with melting temperature for all of the data examined.

The data presented do not include intermetallics which disappear by peritectic reaction. For WC (4), FeTi (5), and Fe_3Si (6) which undergo peritectic decomposition, the measured elastic constants are larger than predicted using the peritectic temperature as the melting temperature. This is particularly true for WC which decomposes by a peritectic reaction at 3050°C. Its $\bar{C}_{ii}$ value, 804 GPA, (8) predicts a melting temperature of 3972°K. On the other hand V_3Si which has the β-W structure disappears by peritectic reaction at approximately 2350°K which lies close to the liquidus temperature. Its C_{11}, 287 GPa, (14) lies above the line in Fig. 1. Thus, the peritectic temperature is not a reliable predictor of the C_{11} type elastic constants.

Acknowledgment

References

1. W.M. Griffith et al., "Elevated Temperature Aluminum Alloys for Aerospace Applications" in High-Strength Powder Metallurgy Aluminum Alloys, M.J. Koczak and G.J. Hildeman, eds., Proc. TMS-AIME Conference, Dallas, (Feb. 17-18, 1982).

2. G. Simmons and H. Wang, Single Crystal Elastic Constants and Calculated Aggregate
   Properties: A Handbook, 2nd ed., MIT Press, Cambridge, Mass., (1971).
3. H.J. McSkimin and W.L. Bond, Phys. Rev. 105, 116 (1957).
4. M. Lee and R.S. Gilmore, J. Mat. Sci. 17, 2657 (1982).
5. U. Buchenan et al., Phys. Rev. B. Cond. Matter 27, 955 (1983).
6. A.R. Buchner and H.D. Kemnitz, Z. Metallk. 72, 575 (1981).
7. S. Sirinski, Acta Met. 4, 164 (1956).
8. R.J. Schultz et al., J. Appl. Phys. 42, 4680 (1971).
9. F.X. Kayser and C. Stassis, Phys. Stat. Solid 64, 335 (1981).
10. D. Butler et al., J. Phys. C (Solid State Physics) 13, 27 (1980).
11. O. Mercier et al., J. Appl. Phys. 51, 1833 (1980).
12. A.S. Edelstein et al., Solid State Comm. 34, 781 (1980).
13. F.R. Eshelman and J.F. Smith, J. Appl. Phys. 49, 3284 (1978).
14. L.R. Testandi and T.B. Bateman, Phys. Rev. 154, 404 (1967).
15. M. Rosen et al., Phys. Rev. 184, 466 (1969).
16. F.R. Eshelman and J.F. Smith, J. Appl. Phys. 46, 5080 (1975).
17. R.J. Schiltz, Jr. and J.F. Smith, J. Appl. Phys. 45, 4681 (1974).
18. G.W. Shannette and J.F. Smith, J. Appl. Phys. 42, 2799 (1971).
19. K. Kuriyama and S. Saito, Phys. Rev. B (Solid State) 13, 1528 (1976).
20. T. Tanaka et al., Solid State Commun. 22, 203 (1977).
21. G.W. Shannette and J.F. Smith, Scripta Met. 3, 33 (1969).
22. Y.C. Akgoz et al., J. Phys. Chem. Solids 34, 131 (1973).
23. D.Y. Chung et al., Physics Letters, 47A, 449 (1974).
24. K. Salama et al., J. Appl. Phys. 44, 180 (1973).
25. J.F. Tonnies et al., J. Appl. Phys. 42, 3275 (1971).
26. J.D. Greiner et al., J. Appl. Phys. 47, 3427 (1976)
27. J.D. Greiner et al., J. Appl. Phys. 44, 3862 (1973).
28. K. Salama et al., J. Appl. Phys. 43, 3254 (1972).
29. E.S. Fisher and D. Dever, Proc. Rare Earth Conference, vol. 7, p. 237, Coronado, CA (1968).
30. J.D. Greiner et al., Scripta Met. 14, 989 (1980).

TABLE I

Data Plotted in Figures 1 and 2

Metal	Data Pt.No.	C_{11} GPa	B GPa	T_m Deg. K	Ref. No.	Metal	Data Pt.No.	C_{11} GPa	B GPa	T_m Deg. K	Ref. No.
Ag	1	124	104	1234	(51)	Al_2Y	24	171	80	1758	17
Al	2	107	76	933	(140)	AuCd	25	83	85	900	7
Au	3	193	173	1336	(51)	AuZn	26	42	56	998	8
Cr	4	350	162	2153	(40)	B_6La	27	453	90	2803	20
Cu	5	170	138	1356	(51)	Co_2Hf	28	256	167	1843	(229)
Fe	6	233	168	1803	(211)	Co_2Zr	29	233	153	1813	(229)
K	7	4	3	337	(239)	Cu_2Mg	30	123	88	1092	(56)
Li	8	14	12	453	(255)	CuZn	31	129	116	1175	(149)
Mo	9	441	268	2898	(89)	LiIn	32	56	47	898	19
Na	10	7	7	371	(67)	MgAg	33	85	66	1093	(56)
Nb	11	246	174	2708	(47)	MgCuZn	34	134	58	1098	18
Ni	12	251	184	1725	(17)	Mg_2Si	35	121	55	1375	(277)
Pb	13	50	45	600	(270)	Mg_2Sn	36	82	41	1051	(70)
Pd	14	227	193	1827	(209)	NiAl	37	212	166	1911	(273)
Pt	15	347	283	2047	(158)	Ni_3Al	38	224	174	1668	9
Ta	16	261	192	3273	(89)	NiTi	39	162	140	1513	11
Th	17	75	58	1950	(21)	Sn_3Ce	40	81	55	1435	12
V	18	229	156	2133	(38)	TaC	41	505	217	4073	(24)
W	19	523	311	3663	(89)	TiC	42	515	242	3523	(49)
Al_2Ca	20	97	47	1352	17	UC	43	320	163	2663	(118)
Al_2Gd	21	161	78	1798	17	V_3Ge	44	297	168	2193	15
Al_2La	22	144	69	1697	17	YZn	45	94	62	1378	8
Al_2U	23	170	83	1863	14	ZrC	46	472	168	3450	(49)

TABLE II
Data Plotted in Figure 3

Metal	C_{11}	T_m	Ref
Ge	129	1211	(163)
Si	166	1687	(164)
AlSb	89	1338	(42)
GaAs	118	1511	(99)
GaP	141	1740	(276)
GaSb	89	979	(170)
InAs	87	1215	(215)
InP	102	1331	(131)
InSb	67	803	(27)

TABLE III
Data Plotted in Figure 4

| tal	C_{ii} GPa	T_m Deg K	Ref	Metal	C_{ii} GPa	T_m Deg K	Ref
Bi	55	544	(81)	Zr_2Ni	152	1413	16
Cd	93	594	(50)	Be	307	1553	(237)
Co	323	1768	(94)	Tl	45	576	(90)
In	45	430	(48)	Dy	86	1685	(94)
Mg	60	923	(236)	Er	86	1802	(94)
Re	637	3450	(230)	Gd	68	1586	(93)
Ru	583	2600	(94)	Ho	77	1734	24
Sb	81	903	(86)	Ln	85	1925	25
Zn	130	693	(16)	Nd	57	1297	26
$_2Al$	151	1053	(53)	Pr	52	1204	26
$_2Cu$	177	864	13	Tb	69	1629	27
$_2Ti$	607	3253	(112)	Hf	186	2463	(95)
Bi	46	383	22	Sc	102	1812	28
$_2Bi$	58	362	23	Ti	169	1933	(95)
$_2Ca$	58	987	(248)	Y	78	1795	(238)
$_5Ce$	232	1588	10	Zr	151	2125	(95)
$_2Mg$	108	863	21				

erences in parentheses are from Simmons and Wang (2).
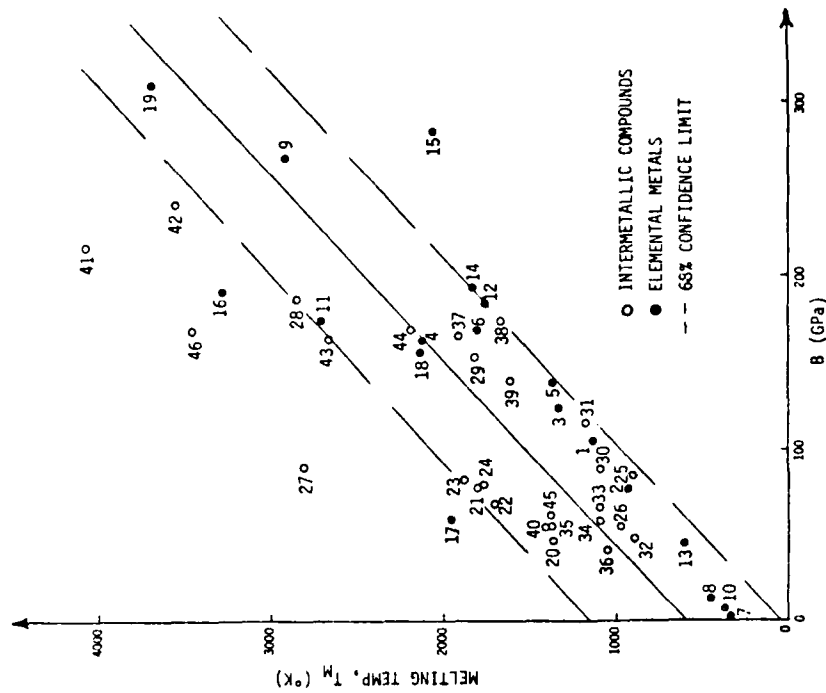
Fig. 2. Bulk modulus versus melting temperature for cubic elemental metals and intermetallic compounds. The line plotted is a least squares fit to the data with the dashed lines the 68% confidence level. The elements and intermetallics are identified by number in Table I.
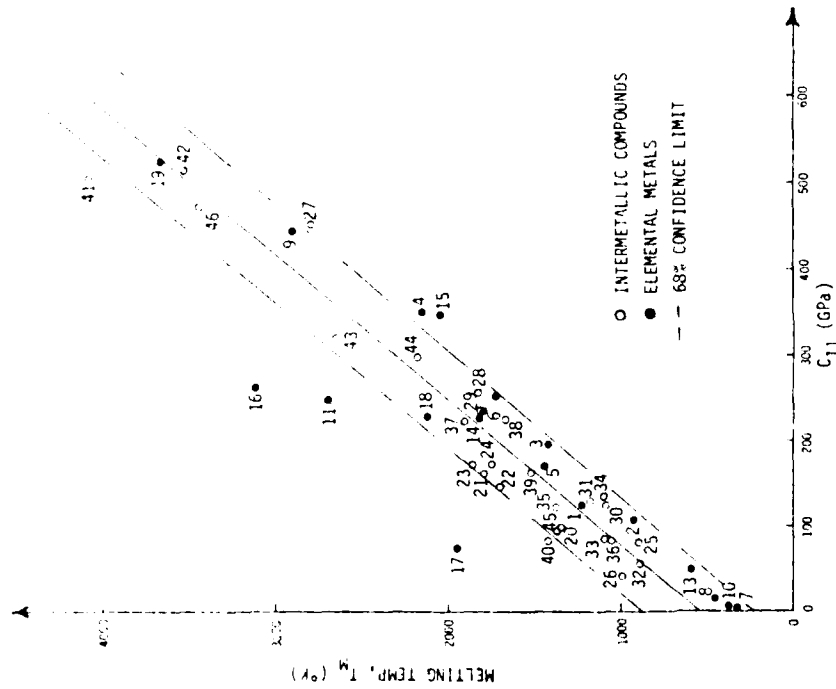

Fig. 1. C_{11} elastic constant versus melting temperature for cubic elemental metals and intermetallic compounds. The line plotted is a least squares fit to the data with the dashed lines the 68% confidence level. The numbers refer to the data given in Table I.
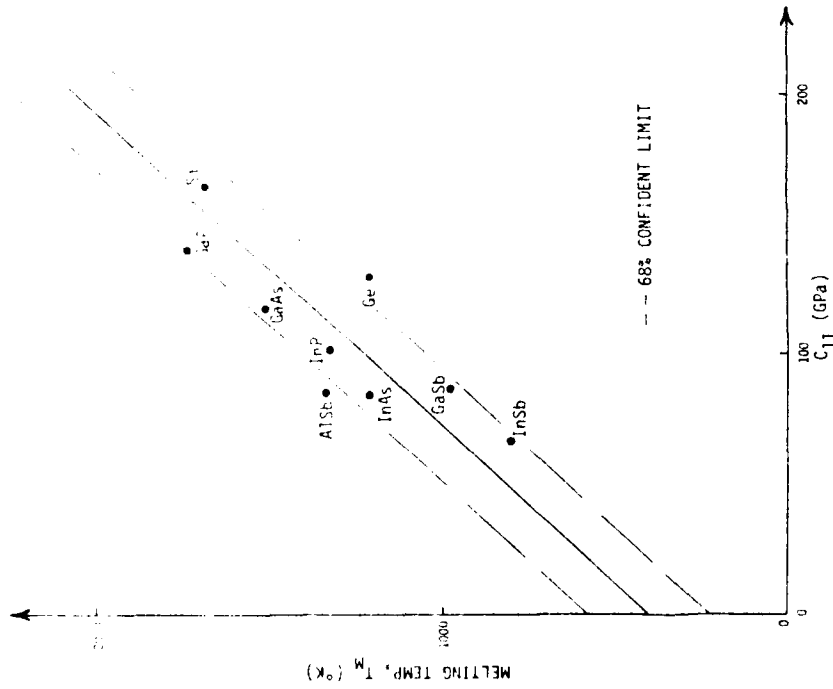
Fig. 4. $\bar{C}_{ii}$ versus T_m for hexagonal and tetragonal elemental metals and intermetallic compounds. The data are given in Table III. The least squares line utilized only the open and closed circles with the dashed lines the 68% confidence level.

Fig. 3. C_{11} for Si, Ge and III-IV semiconductors vs T_m. The data are given in Table II. The line is a least squares fit to the data with the dashed lines the 68% confidence level.
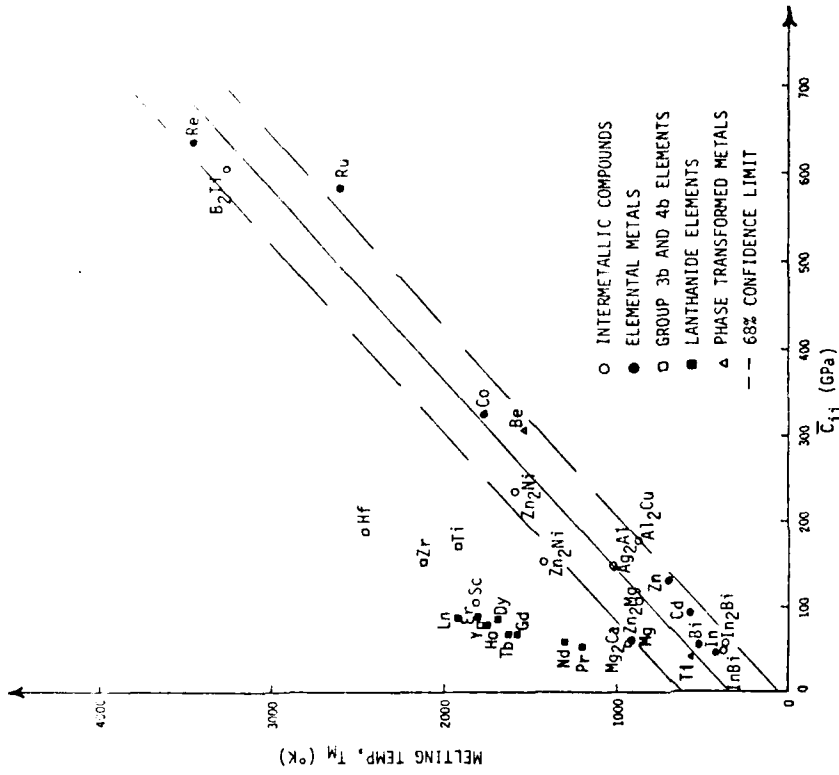
END

FILMED

5-85

DTIC